Supporting information

Identifying high performance and durable methylammonium-free lead halide perovskites through high throughput synthesis and characterization

Yu An [a, b, c], Carlo Andrea Riccardo Perini [b], Juanita Hidalgo [b], Andrés-Felipe Castro-Méndez [b], Jacob N. Vagott [b], Ruipeng Li [d], Wissam Saidi [e], Shirong Wang [a,c], Xianggao Li [a,c] and Juan-Pablo Correa-Baena [b]**

[a] School of Chemical Engineering and Technology, Tianjin University, Tianjin, 300072, China

[b] School of Materials Science and Engineering, Georgia Institute of Technology, Atlanta, Georgia, 30332, United States

[c] Collaborative Innovation Center of Chemical Science and Engineering (Tianjin), Tianjin, 300072, China

[d] National Synchrotron Light Source II, Brookhaven National Lab, Upton, New York, 11973, United States

[e] Department of Mechanical Engineering and Materials Science, University of Pittsburgh, Pittsburgh, PA 15261, USA

*Corresponding Authors: X. Li lixianggao@tju.edu.cn; JPCB jpcorrea@gatech.edu

I. Experimental materials and methods

Materials

Lead iodide (PbI_2) and lead bromide ($PbBr_2$) were purchased from TCI America. Formamidinium iodide (FAI) and formamidinium bromide (FABr) were purchased from Dyenamo. 2,2',7,7'-Tetrakis[N,N-di(4-methoxyphenyl)amino]-9,9'-spirobifluorene (spiroOMeTAD) was purchased from 1-Material. Dimethylformamide (DMF), dimethyl sulfoxide (DMSO) and chlorobenzene (CB) were purchased from Acros Organics. Cesium iodide (CsI), cesium bromide (CsBr), titanium diisopropoxide bis(acetylacetonate) (75 wt. % in isopropanol), acetylacetone, anhydrous ethanol (EtOH), titanium dioxide paste (TiO_2, 30 NR-D), lithium bistrifluorosulfonyl imide (Li-TFSI), tris(2-(1H-pyrazol-1-yl)-4-tert-butylpyridine)cobalt(III) tri[bis(trifluoromethane)sulfonimide] (FK 209 Co(III) TFSI), 4-tertbutyl pyridine (tBP), acetonitrile were bought from Sigma-Aldrich. Au pellets were purchased from Kurt J. Lesker. All the chemicals were used as received without further purification. Conductive glass, fluorine-tin-oxide (FTO) coated (10 ohms/sq, 1-inch × 1-inch), was purchased from Kintec.

Perovskite active layer deposition

Preparation of 0.4 M perovskite precursor solutions: Due to the poor solubility of CsBr in DMF and DMSO, 0.4 M perovskite precursor solutions were prepared for all 49 compositions. Four master solutions were used to prepare a total of 49 precursor solutions with varying ratios of Cs/FA and Br/I. The master solutions were 0.4 M $CsPbI_3$, $FAPbI_3$, $CsPbBr_3$, and $FAPbBr_3$, which were synthesized by dissolving stoichiometric CsI and PbI_2, FAI and PbI_2, CsBr and $PbBr_2$, FABr and $PbBr_2$ in DMSO, respectively. The perovskite precursor solutions were prepared in a N_2 glovebox with < 2 ppm of O_2 and H_2O under the mild heating condition at ~65 °C for 1 h to assist dissolving. These four solutions were mixed in the right molar ratios to yield the other 45 stoichiometric solutions with the desired $Cs_yFA_{1-y}Pb(Br_xI_{1-x})_3$ compositions.

Fabrication of perovskite thin-films from 0.4 M perovskite precursor solutions: The 0.4 M precursor perovskite solution was freshly spin-coated on a substrate pre-heated at 65°C by a two-step spin-coating process, dynamically adding CB as the antisolvent. The first step was carried out at 500 rpm with an acceleration rate of 250 rpm/s for 10 s. The second step followed at 2000 rpm with an acceleration rate of 1000 rpm/s for 70 s. CB (250 μL) was gently dripped at 5 s before the

second step end. All films were then annealed at 65°C for 10 min with the exception of $CsPbI_3$ (65°C for 1 min).

Preparation of 1.0 M perovskite precursor solutions: Four compositions (i.e. $Cs_{2/6}FA_{4/6}PbI_3$, $Cs_{2/6}FA_{4/6}PbBr_{5/2}I_{1/2}$, $Cs_{1/6}FA_{5/6}PbI_3$ and $Cs_{1/6}FA_{5/6}PbBr_{5/2}I_{1/2}$) were selected to increase the concentration from 0.4 M to 1.0 M to improve the photovoltaic performance. 1 M perovskite precursor solutions of $Cs_{2/6}FA_{4/6}PbI_3$ and $Cs_{1/6}FA_{5/6}PbI_3$ were prepared by dissolving a mixture of PbI_2, FAI, and CsI with 5% excess stoichiometry of PbI_2 in a mixed solvent of DMF and DMSO [DMF (v) : DMSO (v) = 4:1]. 1 M perovskite precursor solutions of $Cs_{2/6}FA_{4/6}PbBr_{5/2}I_{1/2}$ and $Cs_{1/6}FA_{5/6}PbBr_{5/2}I_{1/2}$ were prepared by dissolving a mixture of PbI_2, $PbBr_2$, FAI, and CsI with 5% excess stoichiometry of PbI_2 and $PbBr_2$ in a mixed solvent of DMF and DMSO [DMF (v) : DMSO (v) = 4:1]. The perovskite precursor solutions were prepared in a N_2 glovebox with < 2 ppm of O_2 and H_2O under the mild heating condition at ~70 °C for 1 h to assist dissolving.

Fabrication of perovskite thin-films from 1.0 M perovskite precursor solutions: The 1.0 M precursor perovskite solution was spin-coated on the substrate. Spin-coating parameters are two steps, 1000rpm 10 seconds (1000 rpm/s) followed by 6000rpm 20 seconds (2000 rpm/s). CB was gently added 5 s before the end of the second step. The films were then annealed at 150 °C for 10 min.

Device fabrication

Etched FTO-coated glass was sequentially cleaned by sonication in a detergent solution (2% Hellmanex in deionized water), deionized water, acetone, and isopropanol for 15 min to each solvent. After drying with N_2, the substrates were treated under ultraviolet-ozone for 15 min to remove the last traces of organic residues before the deposition of the electron-transporting layer. A compact TiO_2 (c-TiO_2) layer was deposited on the top of FTO-coated glass by spray pyrolysis of a precursor solution of 480 µL acetylacetone and 720 µL titanium diisopropoxide bis(acetylacetonate) (75 wt. % in isopropanol) diluted in 10.8 mL of anhydrous ethanol. The solution was sprayed on the substrates preheated at 450 °C using O_2 as the carrier gas with a 30 s interval between each cycle. The FTO/c-TiO_2 substrates were kept at 450 °C for 30 minutes after finishing the spray procedure then left cool down to ambient temperature. Next, a mesoporous TiO_2 (m-TiO_2) layer was coated on the top of the FTO/c-TiO_2 substrate by spin-coating a 150 mg/mL diluted TiO_2 paste (30 NR-D) in anhydrous ethanol for 10 s at 4000 rpm with a ramp rate

of 4000 rpm s^{-1}. After drying at 100 °C, the as-prepared FTO/c-TiO_2/m-TiO_2 stack was sintered at 450 °C for 30 min. The perovskite layer was deposited on the substrate right after completing the annealing process. A perovskite active layer was deposited by spin-coating a perovskite precursor solution in a N_2 glovebox as mentioned in the "Perovskite active layer deposition" section. The hole-transporting layer was deposited by spin-coating a solution consisting of 91.4 mg of Spiro-OMeTAD, 36.1 µL of tBP, 20.7 µL Li-TFSI (1.8 M in acetonitrile), 9.0 µL of Co(III) TFSI solution (0.25 M in acetonitrile), and 1 mL CB. The concentration of Spiro-OMeTAD solution was 70 mM and the molar ratio of Spiro-OMeTAD : Co(III) TFSI : Li-TFSI : tBP was 1 : 0.03 : 0.5 : 3.3. The 80 µL doped Spiro-OMeTAD solution was dynamically spin-coated on the surface of the perovskite layer at 3000 rpm for 30 s with the ramp of 3000 rpm/s. Finally, 80 nm of Au electrode was thermally evaporated on the top of the Spiro-OMeTAD layer. The evaporation rate was adjusted to 0.01 Å s^{-1} at the first 1 nm, 0.05 Å s^{-1} for the thickness between 1 nm and 5 nm, 0.1 nm s^{-1} for the thickness between 5 nm and 20 nm, and 0.5 Å s^{-1} for the rest 60 nm.

Characterization

UV-vis absorption measurements were performed on a Varian Cary 5000 UV-Vis/NIR spectrometer with a dual-beam. Steady-state photoluminescence was measured using a Horiba Jobin Yvon Fluorolog 3-2iHR1 fluorometer with a 450 W xenon lamp as the excitation source. The films were oriented at 60° relative to the excitation source to decrease interference from reflected light. Perovskite films for UV-vis absorption and photoluminescence measurements were encapsulated with epoxy resin to prevent degradation due to the exposure to ambient atmosphere. The surface morphology of perovskite films was characterized by a high-resolution field emission scanning electron microscope (SEM, Hitachi SU8010) operating at 5 keV and 10 µA. X-ray diffraction (XRD) patterns were recorded in ambient using Malvern PANalytical Empyrean with $Cu_{k\alpha}$ radiation (1.54 Å wavelength). The XRD patterns were collected in Bragg-Brentano geometry from 2θ = 5-65°. Grazing incidence wide-angle X-ray scattering (GIWAXS) measurements were performed at beamline 11-BM of the National Synchrotron Light Source II at Brookhaven national laboratory. The X-ray beam had an energy of 13.5 keV, 0.2 mm (height) x 0.05 mm (width) size, 1 mrad divergence and an energy resolution of 0.7%. The perovskite films deposited on glass with a size of about 0.5 cm × 0.5 cm were measured at an incidence angle of

0.5° with respect to the substrate plane and an exposure time of 10 s. Data were analyzed based on the SciAnalysis package provided by the beamline.

Current-voltage characteristics were acquired using the Litos Lite characterization system (FLUXiM AG, Switzerland) using the Sinus 70 solar simulator as light source, which is state-of-the-art LED solar simulator with AM1.5G spectrum. The solar cells made from 0.4 M perovskite precursor solutions were encapsulated with epoxy resin while the solar cells made from 1.0 M perovskite precursor solutions were not encapsulated. The solar cells were masked with a black metal mask with a pixel area of 0.0625 cm^2 and were measured in a forward and reverse bias at a scan rate of 10 mV/s under ambient conditions. External quantum efficiency was recorded with a home-built setup, composed of a tungsten-halogen lamp and of an Oriel Apex monochromator illuminator, which were coupled with a Keithley 2300 and calibrated with a Newport silicon photodiode (UV818). The maximum power point (MPP) tracking also was collected for 60 s after measuring current-voltage characteristics under AM1.5G illumination. The stability measurements of the solar cells were performed by Litos system (FLUXiM AG) under a white light-emitting diode with 100 W/m^2 light intensity. Aging was implemented under a continuous flow of N_2 in a closed box at 25 ℃ and no additional encapsulation was used. The active area of device for aging was 0.128 cm^2.

Computational Approach

The first-principles density-functional theory (DFT) calculations were carried out within the Perdew-Burke-Ehrenzhof exchange-correlation functional revised for solids (PBEsol) [1] and projector augmented wave (PAW) pseudopotentials [2,3] as implemented in the Vienna Ab initio Simulation Package (VASP) package. Due to importance of van der Waals interactions in the hybrid perovskites [4], we applied Tkatchenko-Scheffler scheme [5,6]. Computational setup including planewave cutoff, kgrid and energy tolerances are properly chosen as tested before [7]. The pure and mixed perovskite phases are modeled using a supercell approach, namely employing a 2×3×1 for the cubic and tetragonal phase and 1×3×1 for the orthorhombic phase. These supercells allow to realize the different compositions synthesized experimentally. Starting from the $CsPbI_3$, the mixed phase is realized using appropriate Cs for FA or I for Br random substitutions. The organic molecule is inserted with a random orientation in the supercell. Hybrid perovskites are known to have a complex potential energy surface with multiple minima. [8] Thus, in our structural

optimization, we relaxed the atomic positions and the lattice cell while constraining the system to maintain the initial lattice symmetry.

II. Supplementary figures and tables

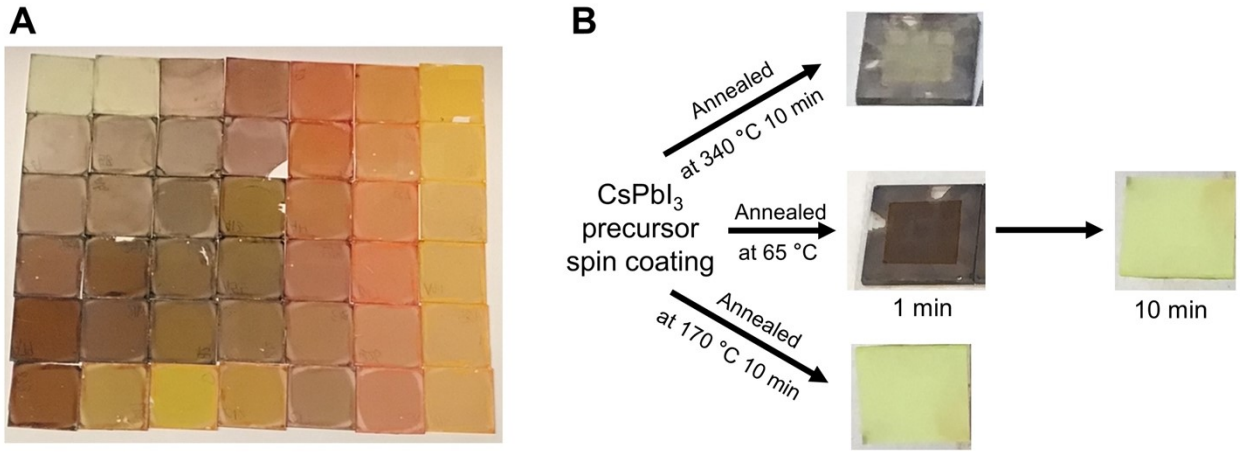

Fig. S1 (A) Photograph of the perovskite films (No.8-No.49) annealed at 170 ℃ for 10 min arranged in the same order as in the composition matrix of Fig. 1A. (B) The different colors of $CsPbI_3$ films annealed at different temperatures.

Crystallographic properties

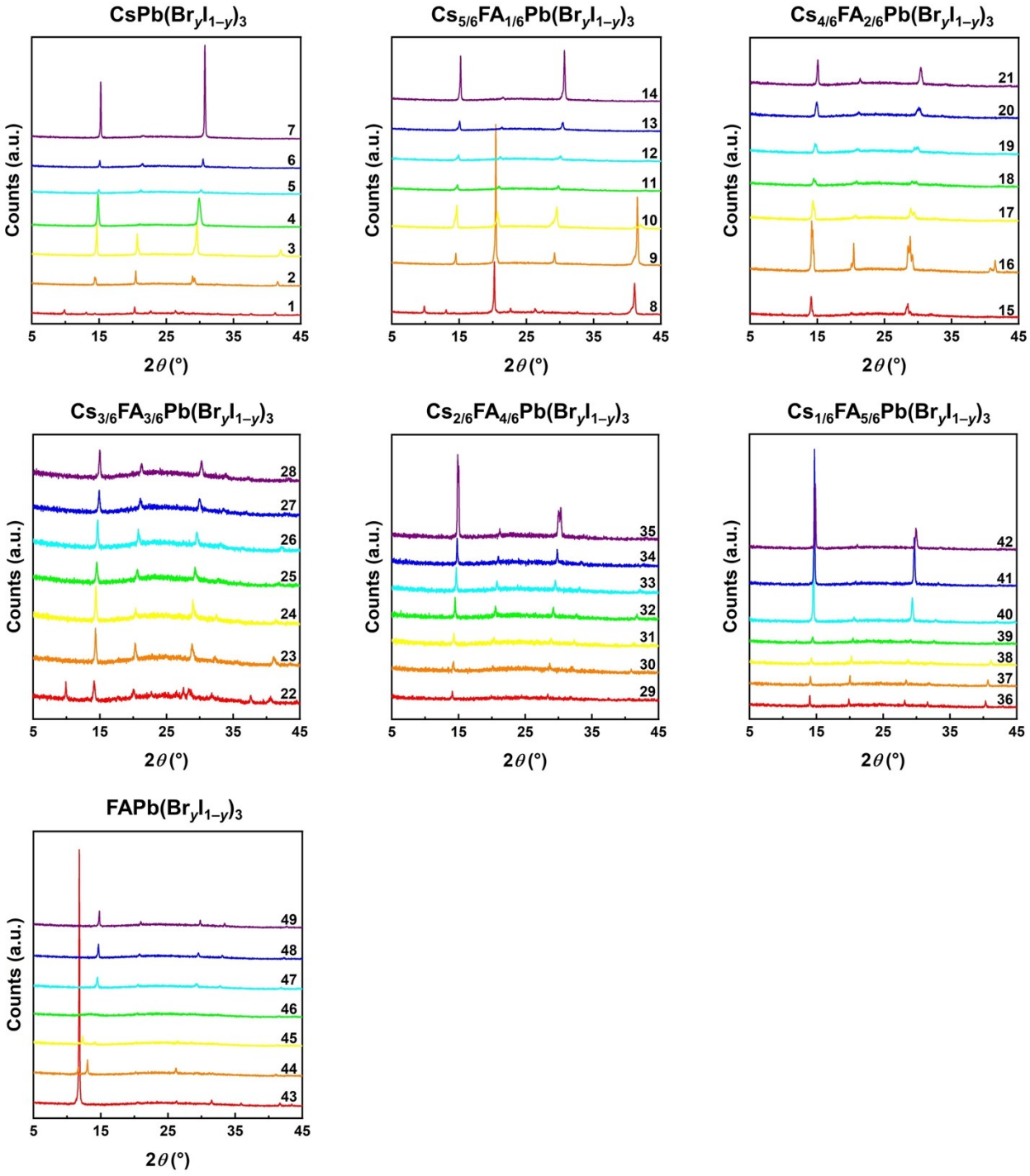

Fig. S2 XRD pattern of 49 compositions compared for the halide ratio. Each figure represents a fixed Cs/FA ratio and a changing Br/I ratio, i.e. every row of the composition matrix.

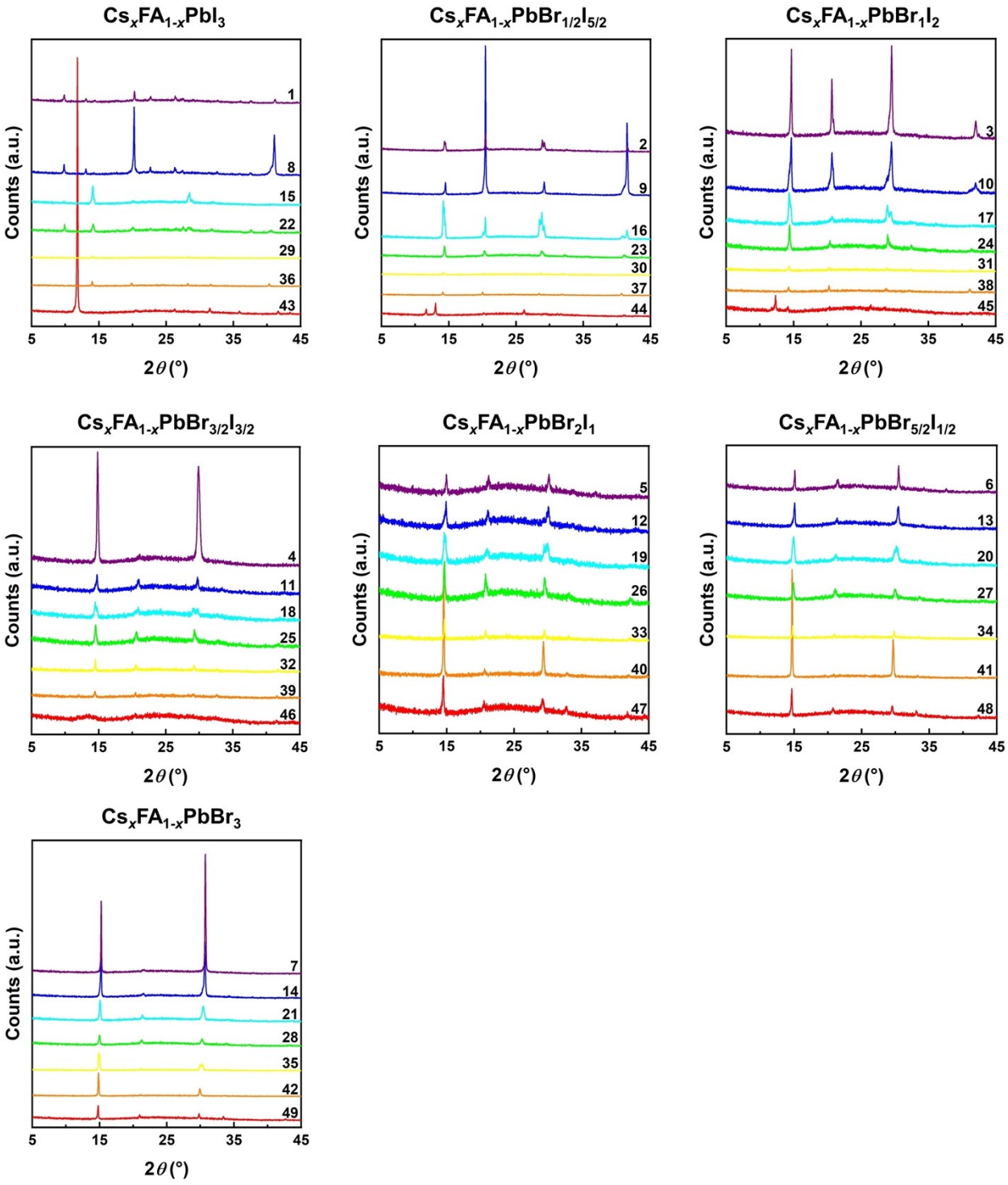

158

159 Fig. S3 XRD pattern of 49 compositions compared for the Cs/FA ratio. Each figure represents a

160 fixed Br/I ratio and a changing Cs/FA ratio, i.e. every column of the composition matrix.

161

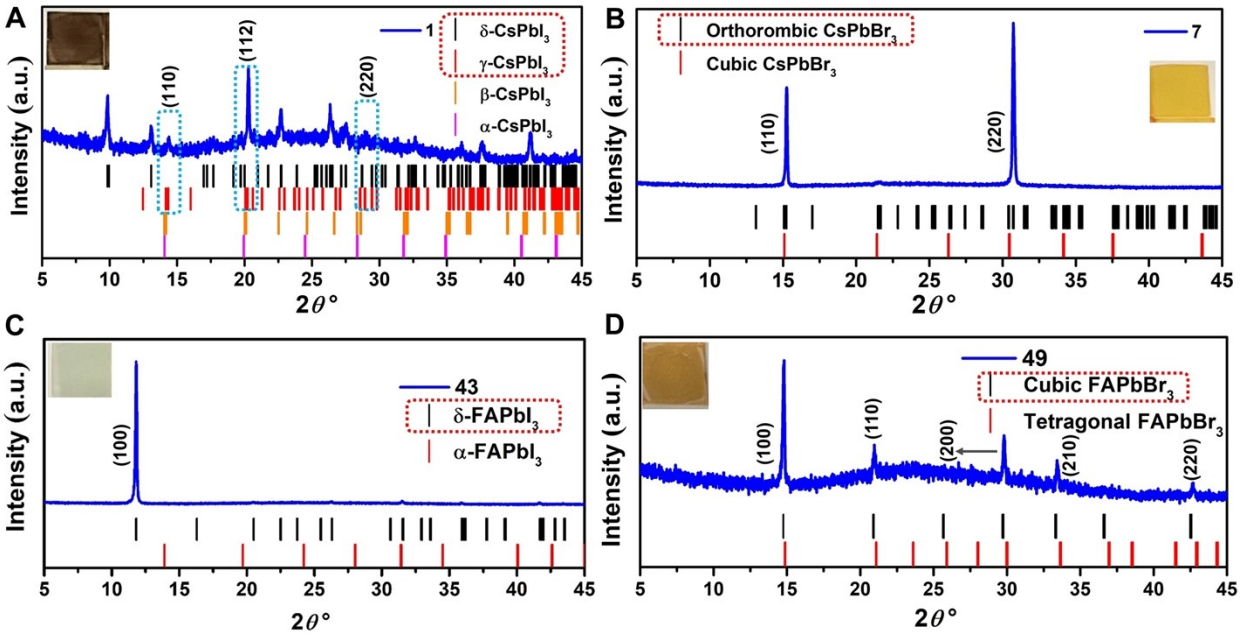

Fig. S4 XRD patterns of four corner compounds, i.e., $CsPbI_3$ (A), $CsPbBr_3$ (B), $FAPbI_3$ (C), and $FAPbBr_3$ (D), compared with the calculated XRD peaks from Vesta software. The crystallographic information files were retrieved from references [9–13].

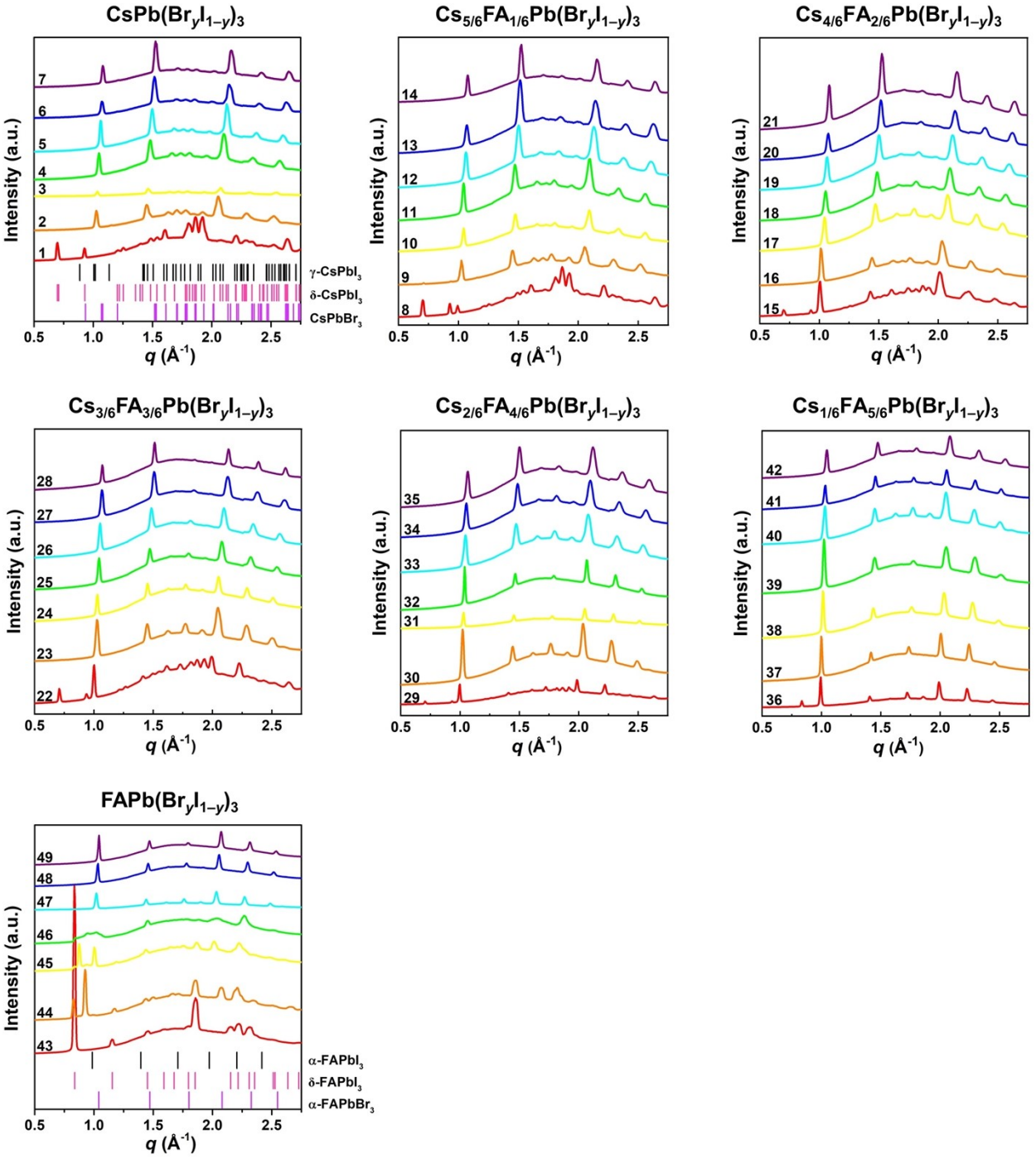

Fig. S5 Circular average of GIWAXS patterns compared for the halide ratio. Each figure represents a fixed Cs/FA ratio and a changing Br/I ratio, i.e. every row of the composition matrix.

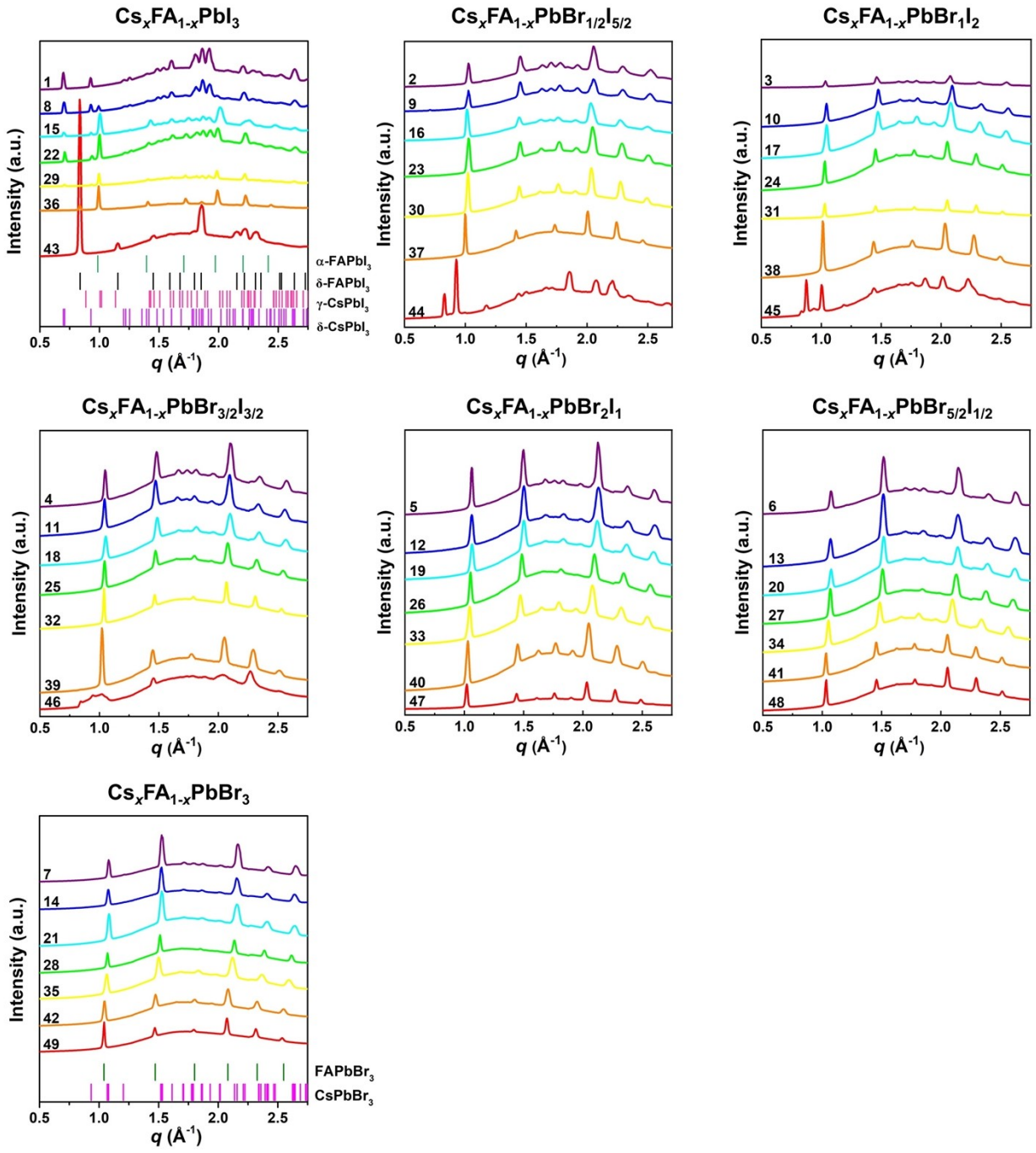

Fig. S6 Circular average of GIWAXS patterns compared for the Cs/FA ratio. Each figure represents a fixed Br/I ratio and a changing Cs/FA ratio, i.e. every column of the composition matrix.

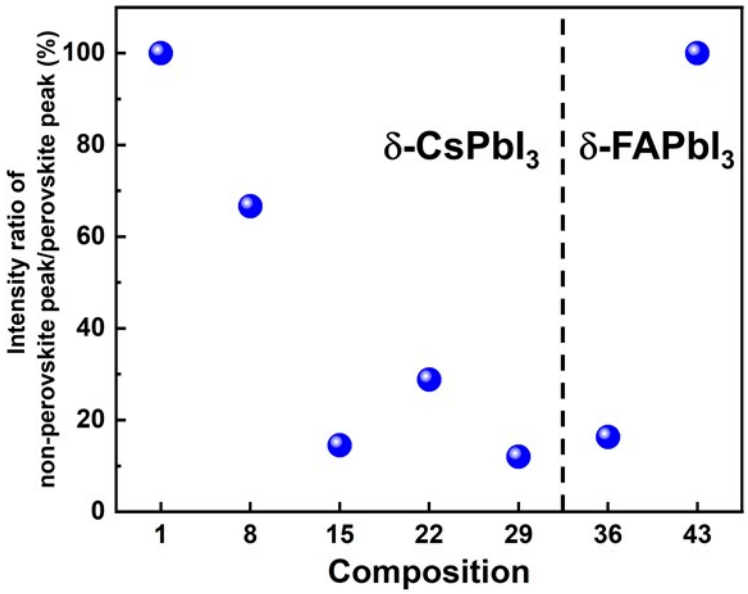

Fig. S7 The calculated intensity ratio of the characteristic peak at q = 0.70 Å^{-1} (δ-$CsPbI_3$) or q = 0.83 Å^{-1} (δ-$FAPbI_3$) for non-perovskite phase over characteristic peak at q around 1.00 Å^{-1} of perovskite phase for $Cs_yFA_{1-y}PbI_3$ compositions based on GIWAXS data.

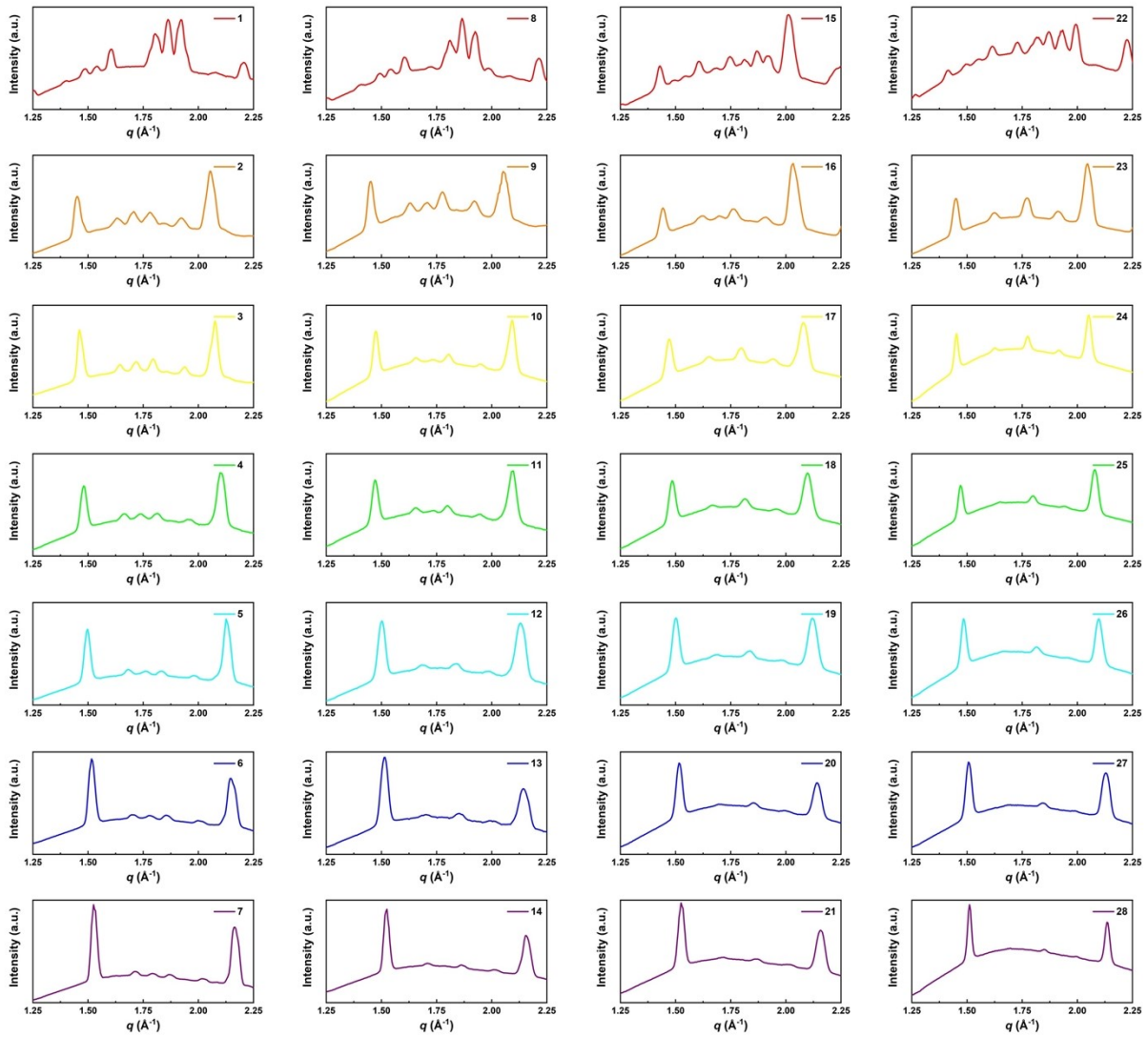

Fig. S8-1 Enlarged circular average of GIWAXS patterns from q = 1.25-2.25 Å^{-1}for composition No.1-28.

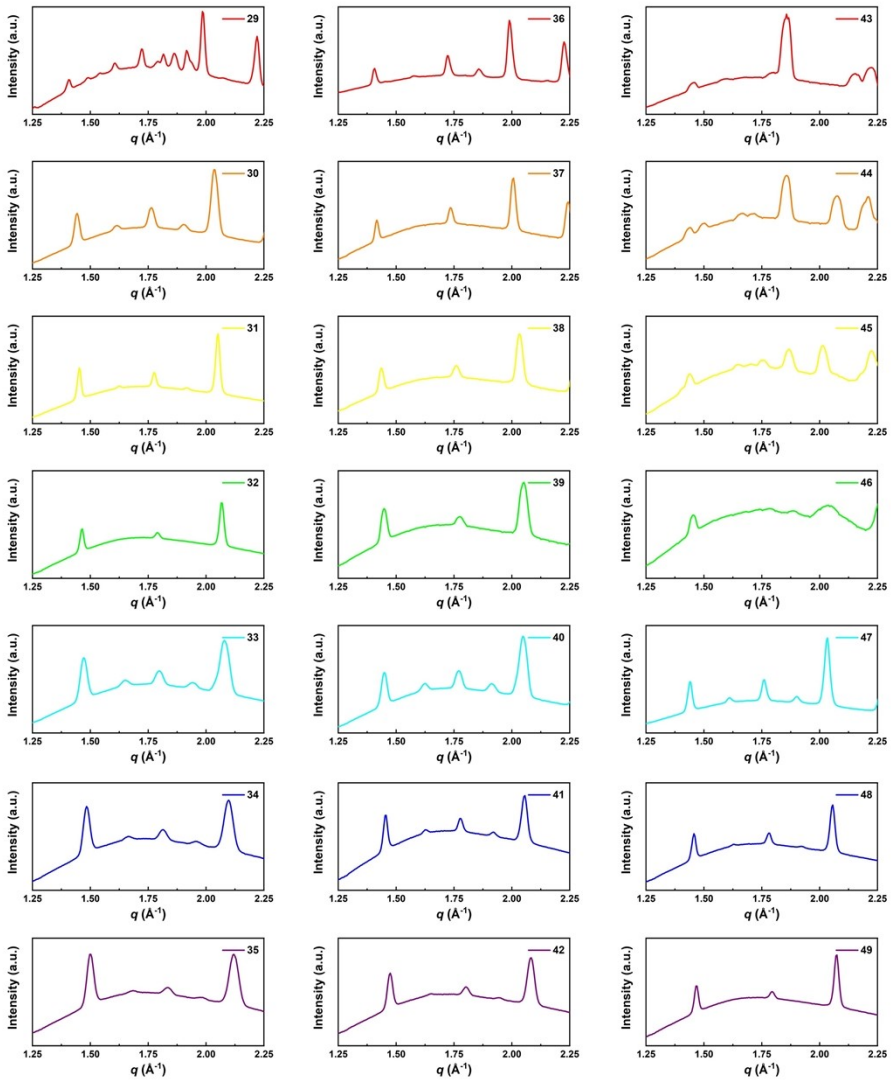

187

188 Fig. S8-2 Enlarged circular average of GIWAXS patterns from q = 1.25-2.25 Å^{-1}for composition

189 No.29-49.

190

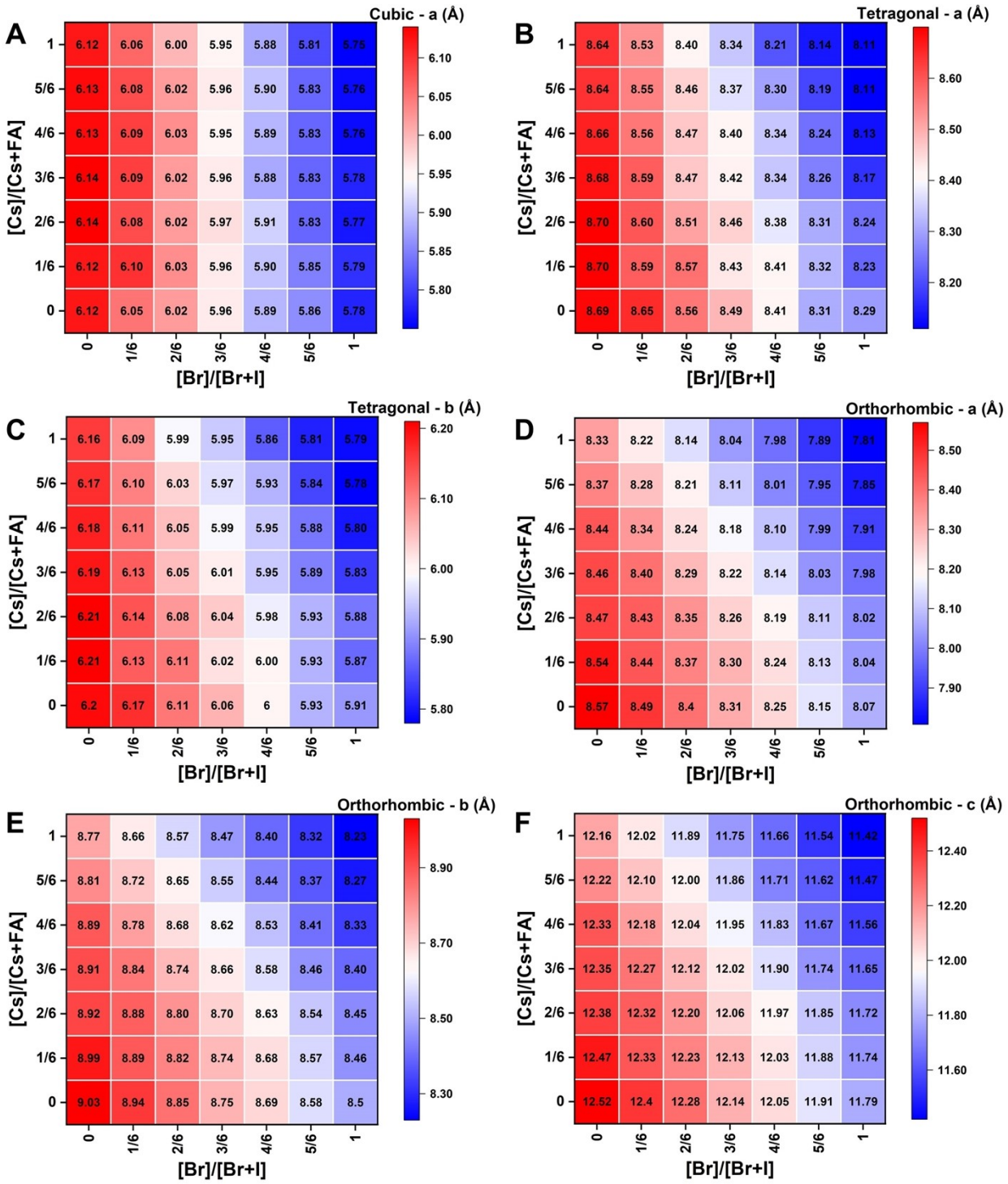

192

193 Fig. S9 The optimized lattice constants for all 49 compositions and for the three phases cubic (A),

194 tetragonal (B and C), and orthorhombic (D-E) calculated by DFT.

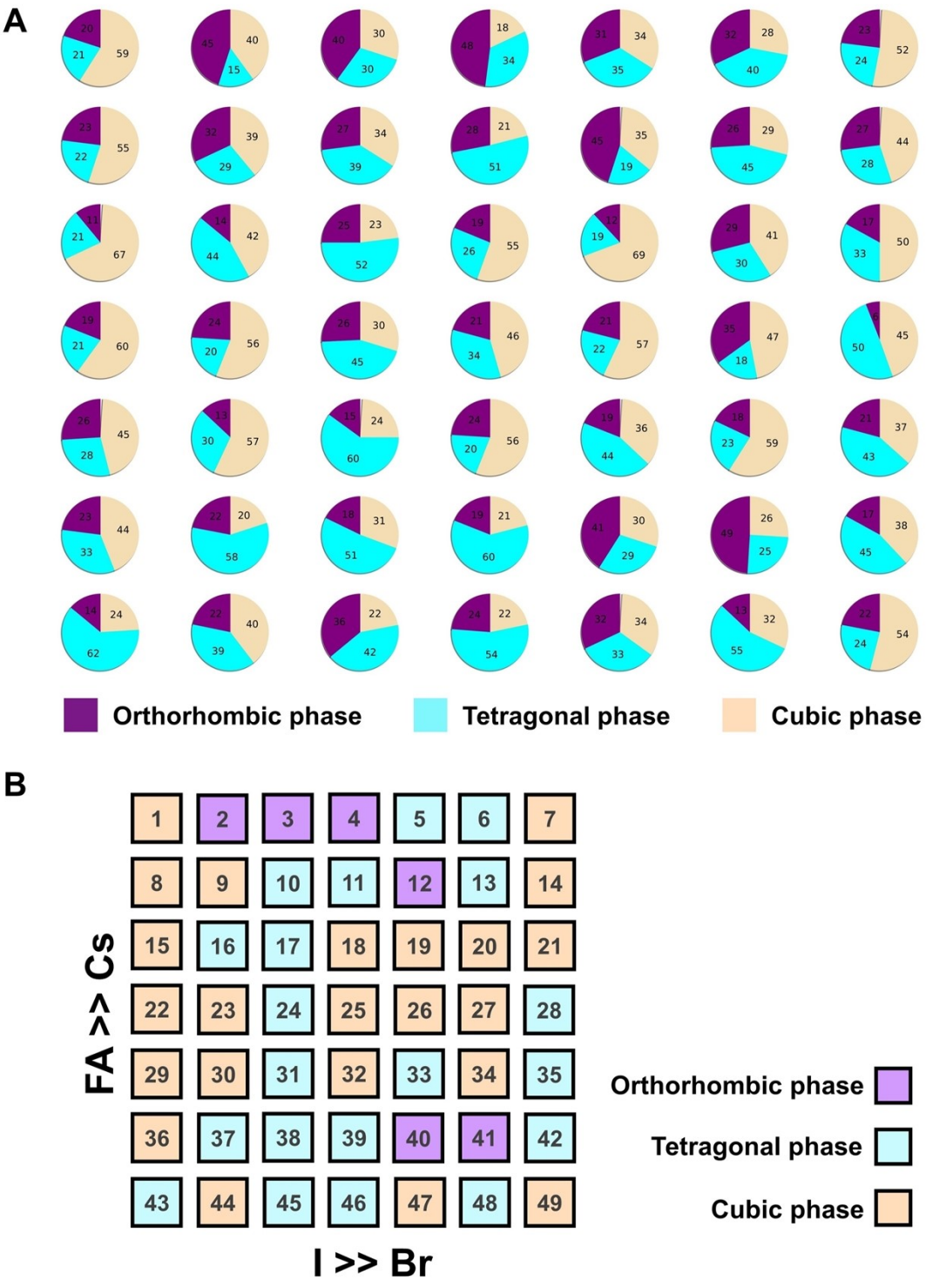

Fig. S10 (A) Thermodynamic stability based on Boltzmann distribution at T = 300°C among cubic, tetragonal and orthorhombic phases for each composition arranged in the same order as in the composition matrix of Fig. 1A. (B) Color map of thermodynamically stable phase at room temperature summarized based on Fig. S9A.

Surface morphology

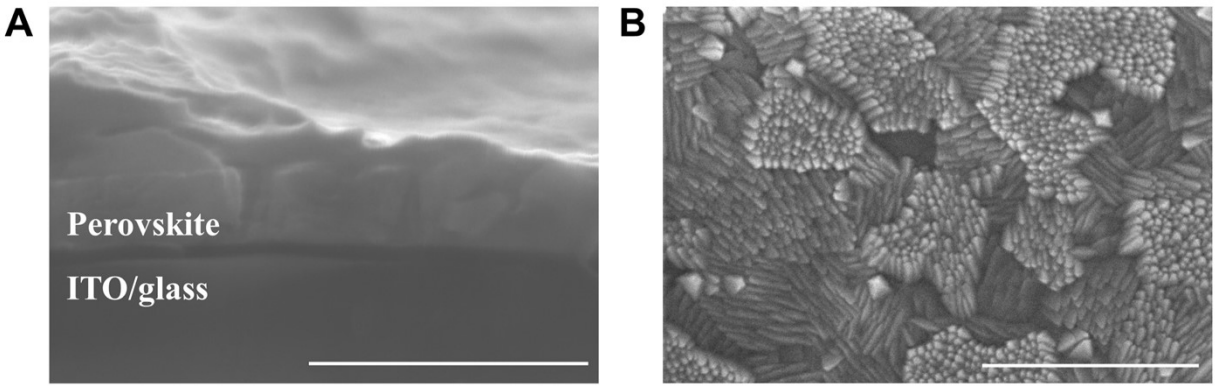

Fig. S11 (A) SEM image of cross-section view of ITO/perovskite layer. The composition of the perovskite layer is $Cs_{1/6}FA_{5/6}PbI_3$. (B) SEM image of the top view of the bare ITO substrate. The white scale bar in these two SEM images are 500 nm**.**

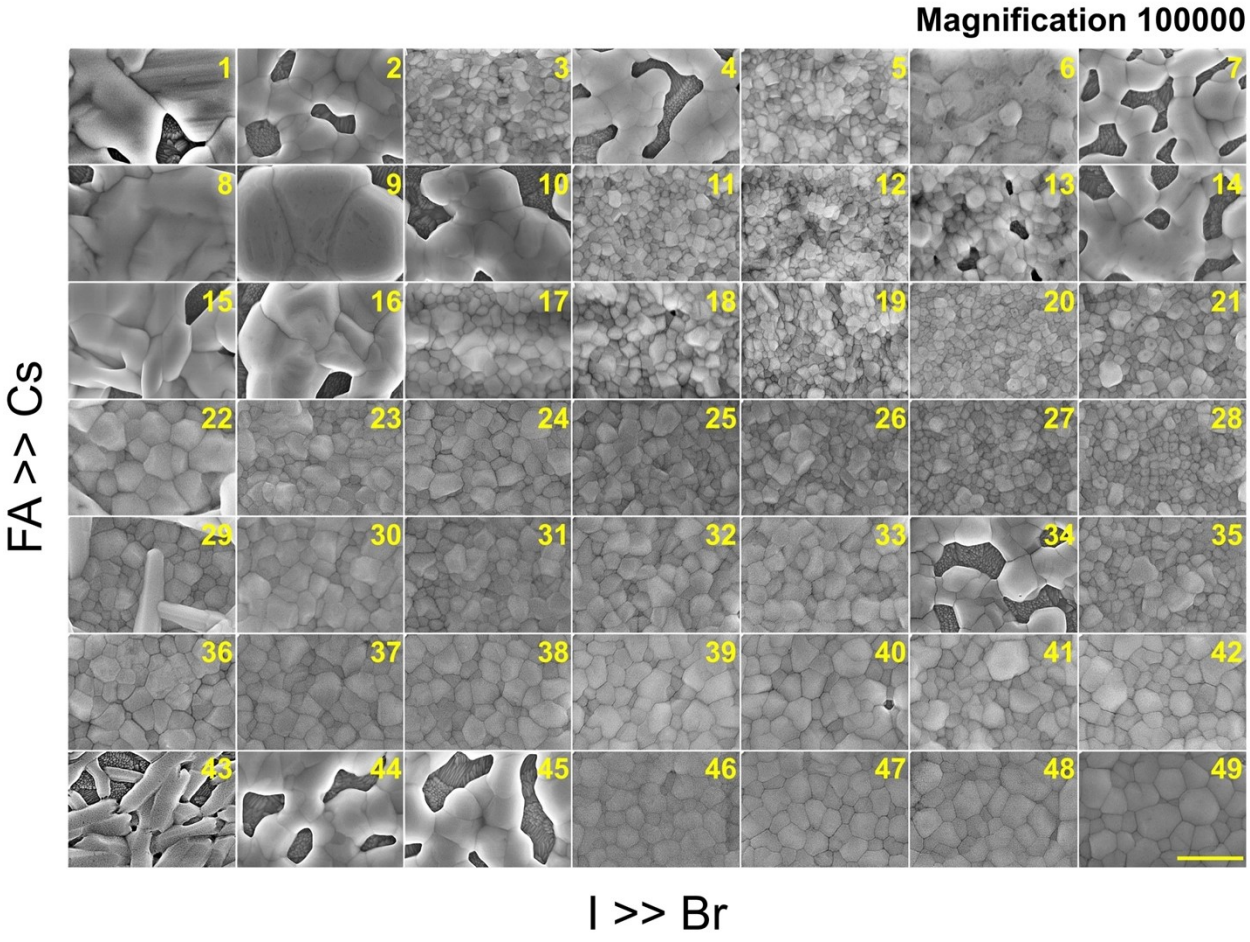

Fig. S12 SEM images of the perovskite films in the $Cs_yFA_{1-y}Pb(Br_xI_{1-x})_3$ compositional space. The panels are arranged in the same order as in the composition matrix of Fig. 1A in the main text. The yellow scale bar on the right bottom is 500 nm.

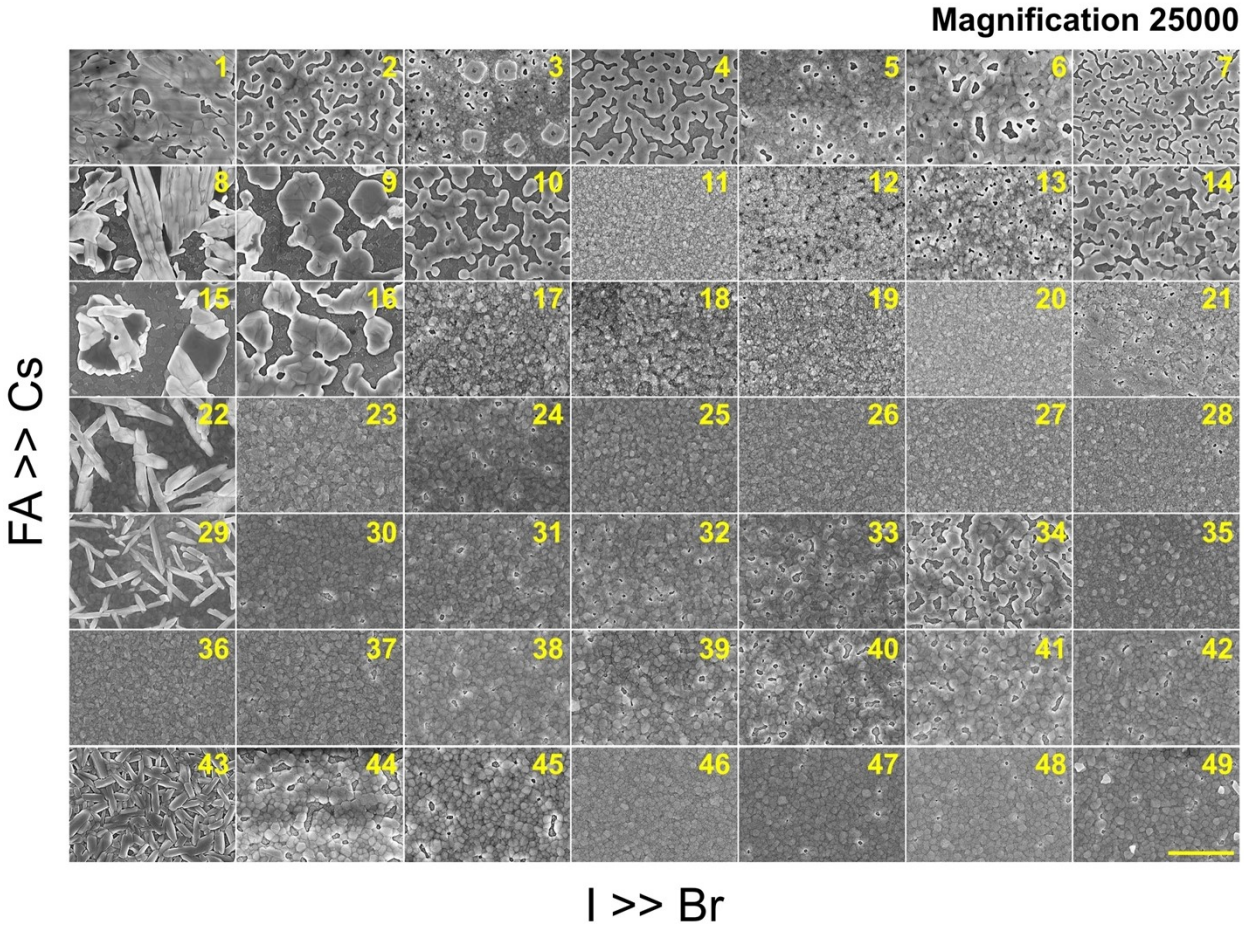

Fig. S13 SEM images of the perovskite films in the $Cs_yFA_{1-y}Pb(Br_xI_{1-x})_3$compositional space. The panels are arranged in the same order as in the composition matrix of Fig. 1A in the main text. The yellow scale bar on the right bottom is 2 μm.

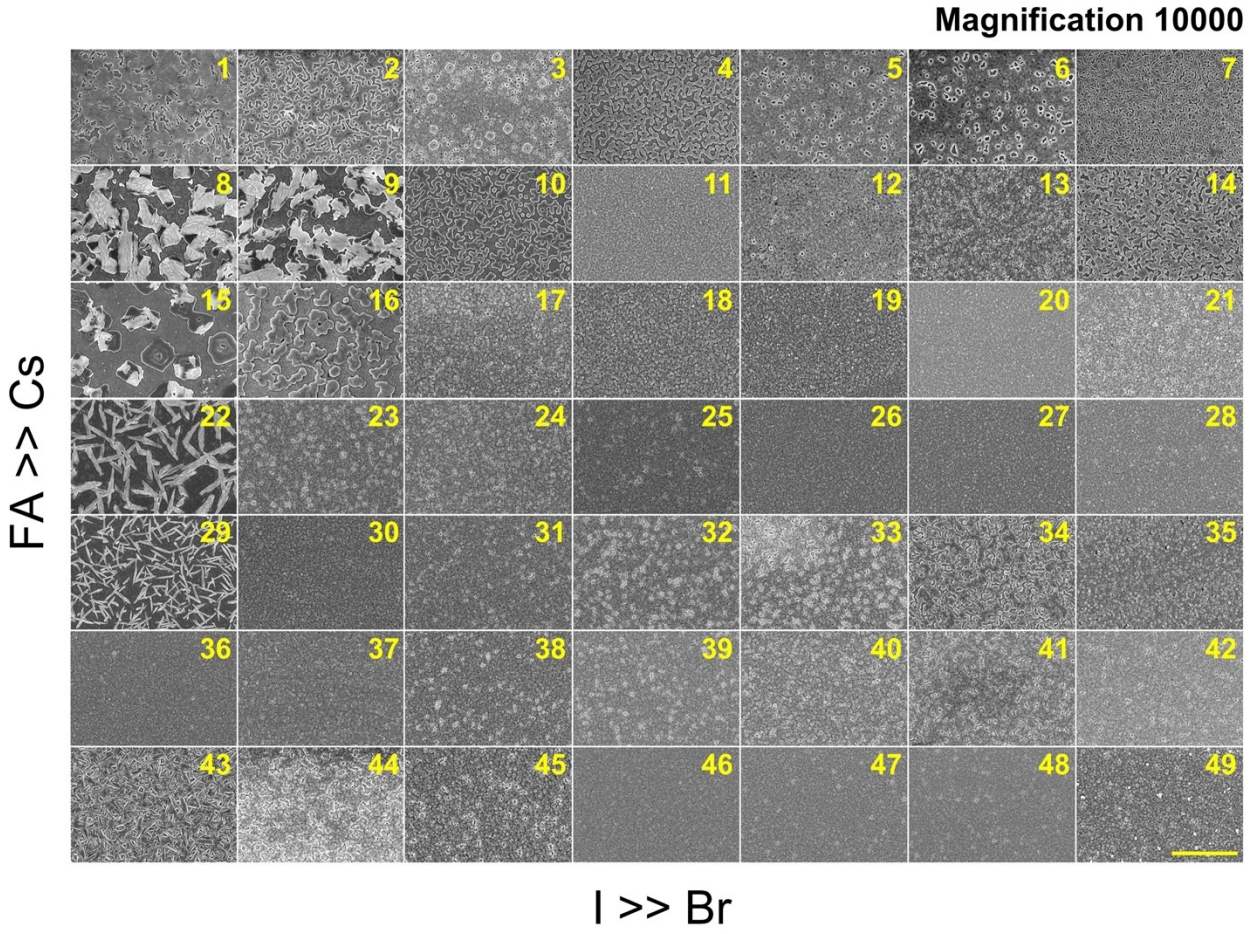

Fig. S14 SEM images of the perovskite films in the $Cs_yFA_{1-y}Pb(Br_xI_{1-x})_3$ compositional space. The panels are arranged in the same order as in the composition matrix of Fig. 1A in the main text. The yellow scale bar on the right bottom is 5 μm.

Optical properties

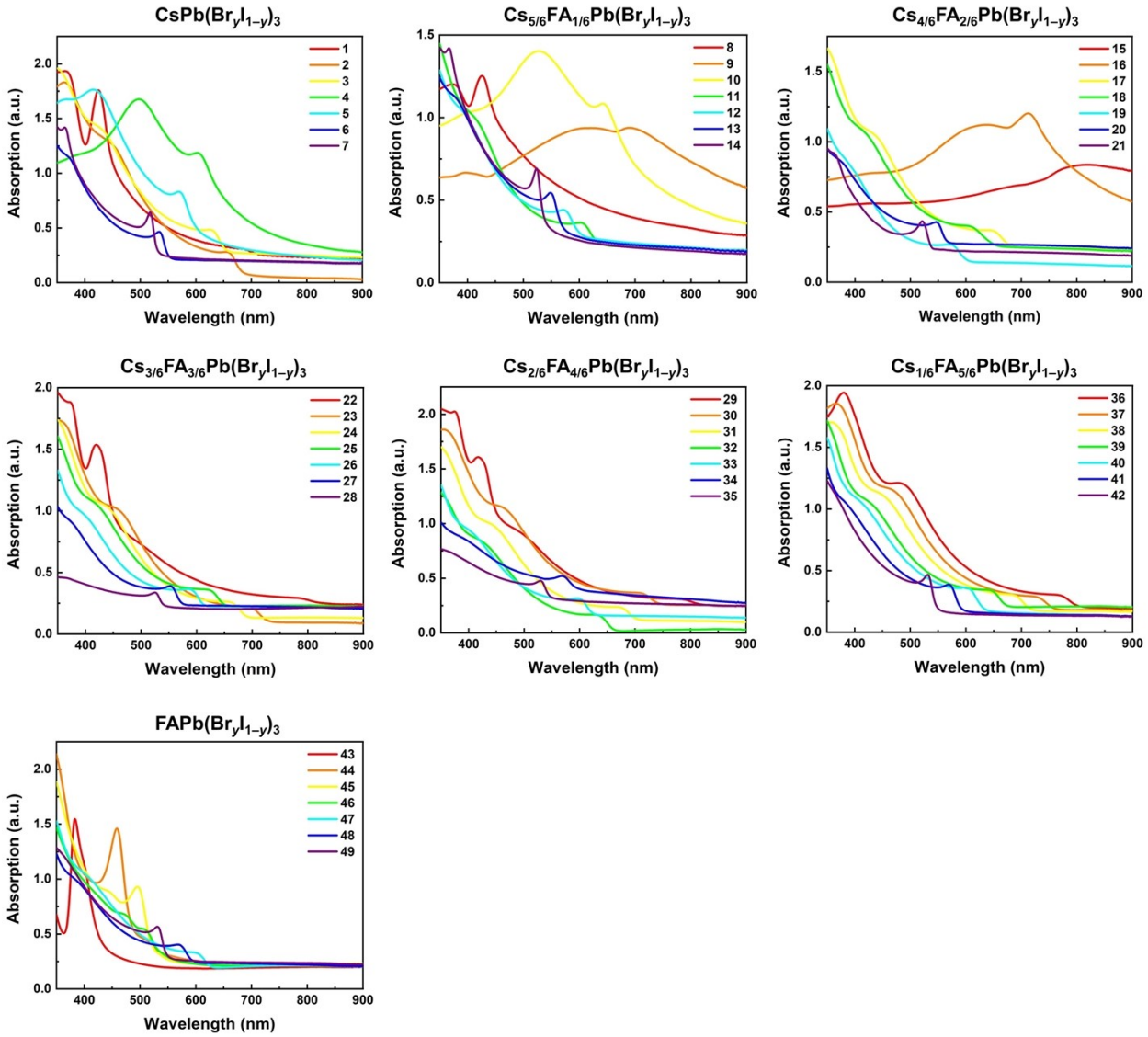

Fig. S15 Ultraviolet-visible absorbance as a function of wavelength. Each figure represents a fixed Cs/FA ratio and a changing Br/I ratio, i.e. every row of the composition matrix.

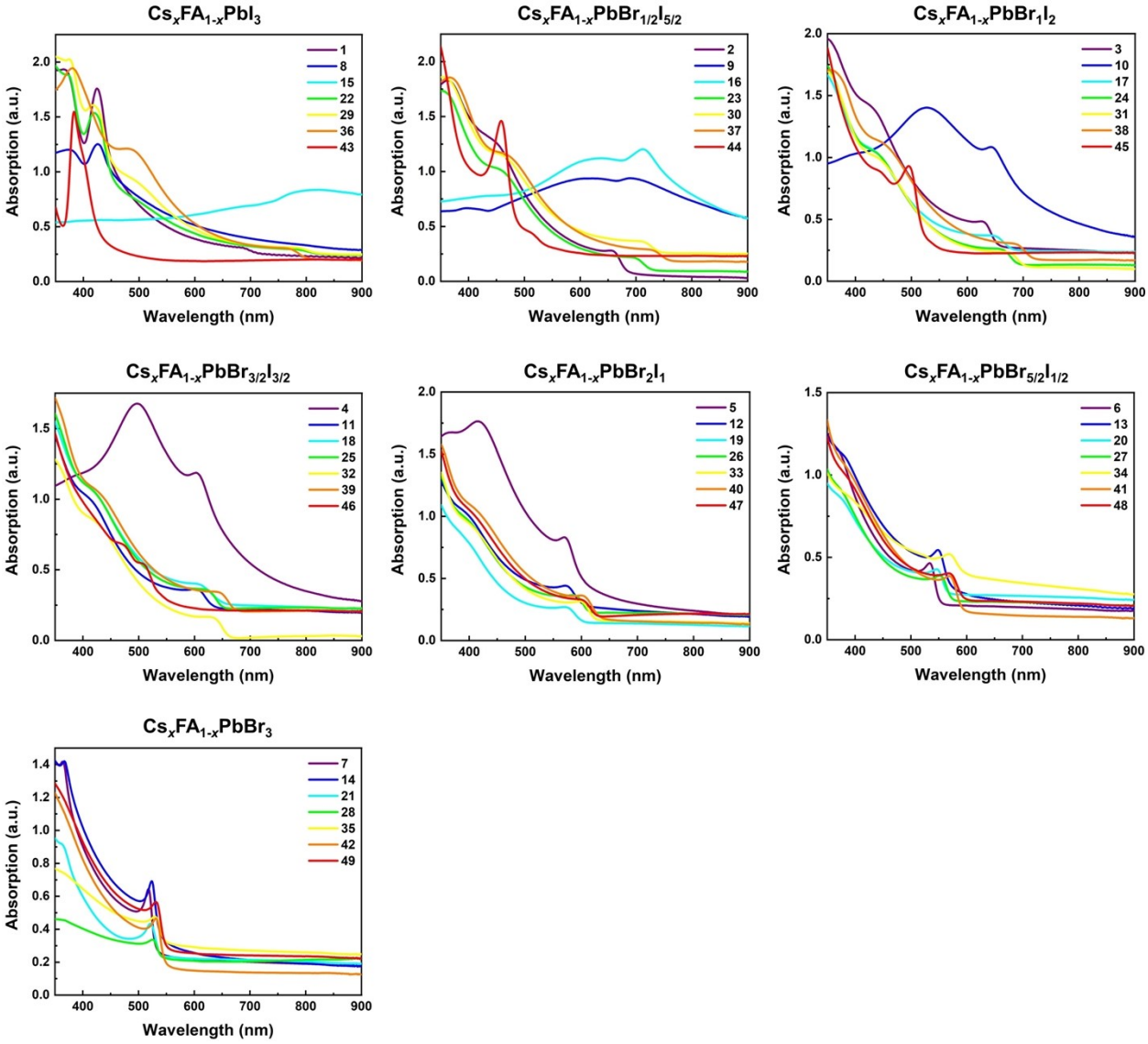

228

229 Fig. S16 Ultraviolet-visible absorbance as a function of wavelength. Each figure represents a fixed

230 Br/I ratio and a changing Cs/FA ratio, i.e. every column of the composition matrix.

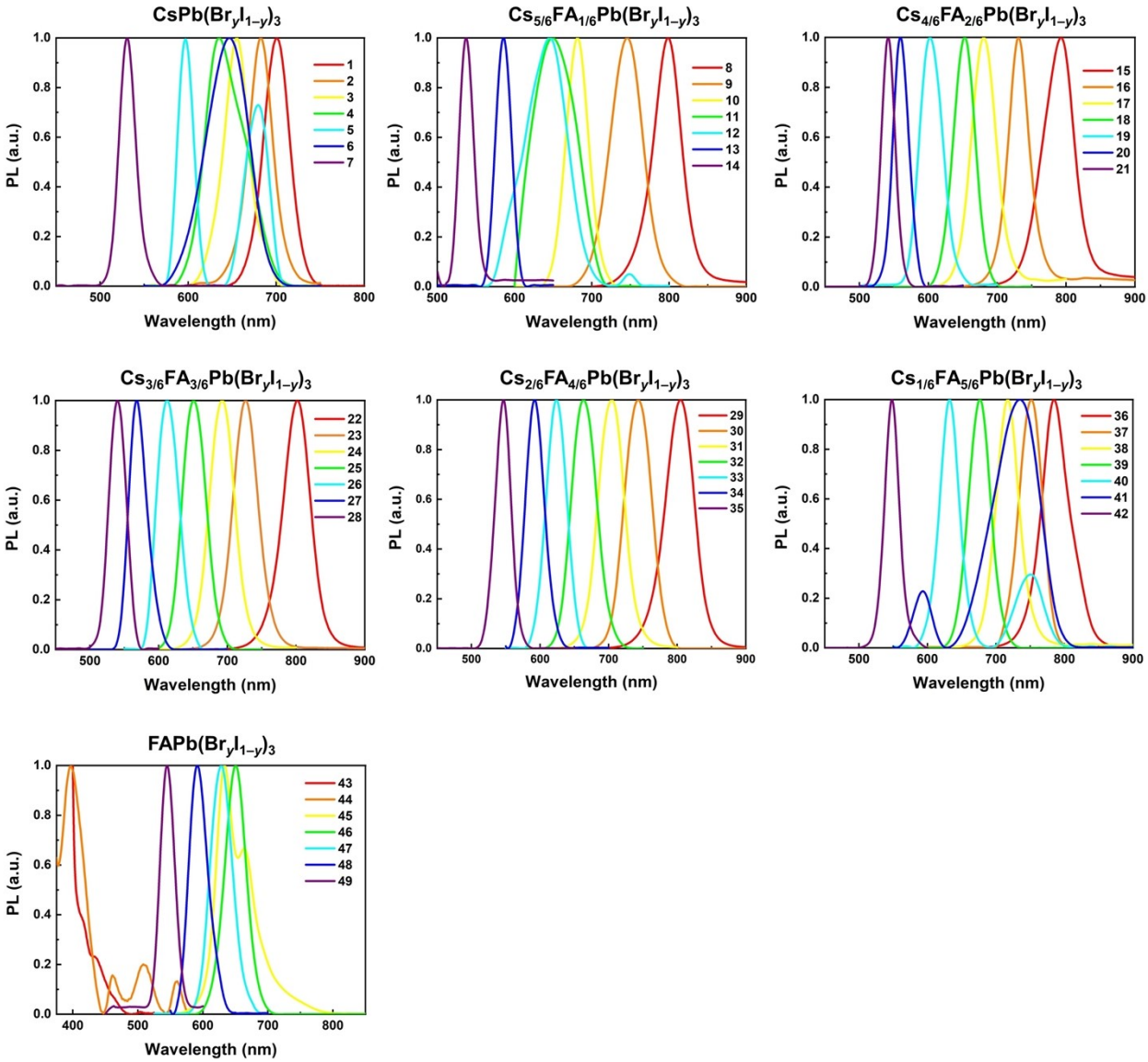

Fig. S17 Normalized photoluminescence spectra as a function of wavelength. Each figure represents a fixed Cs/FA ratio and a changing Br/I ratio, i.e. every row of the composition matrix.

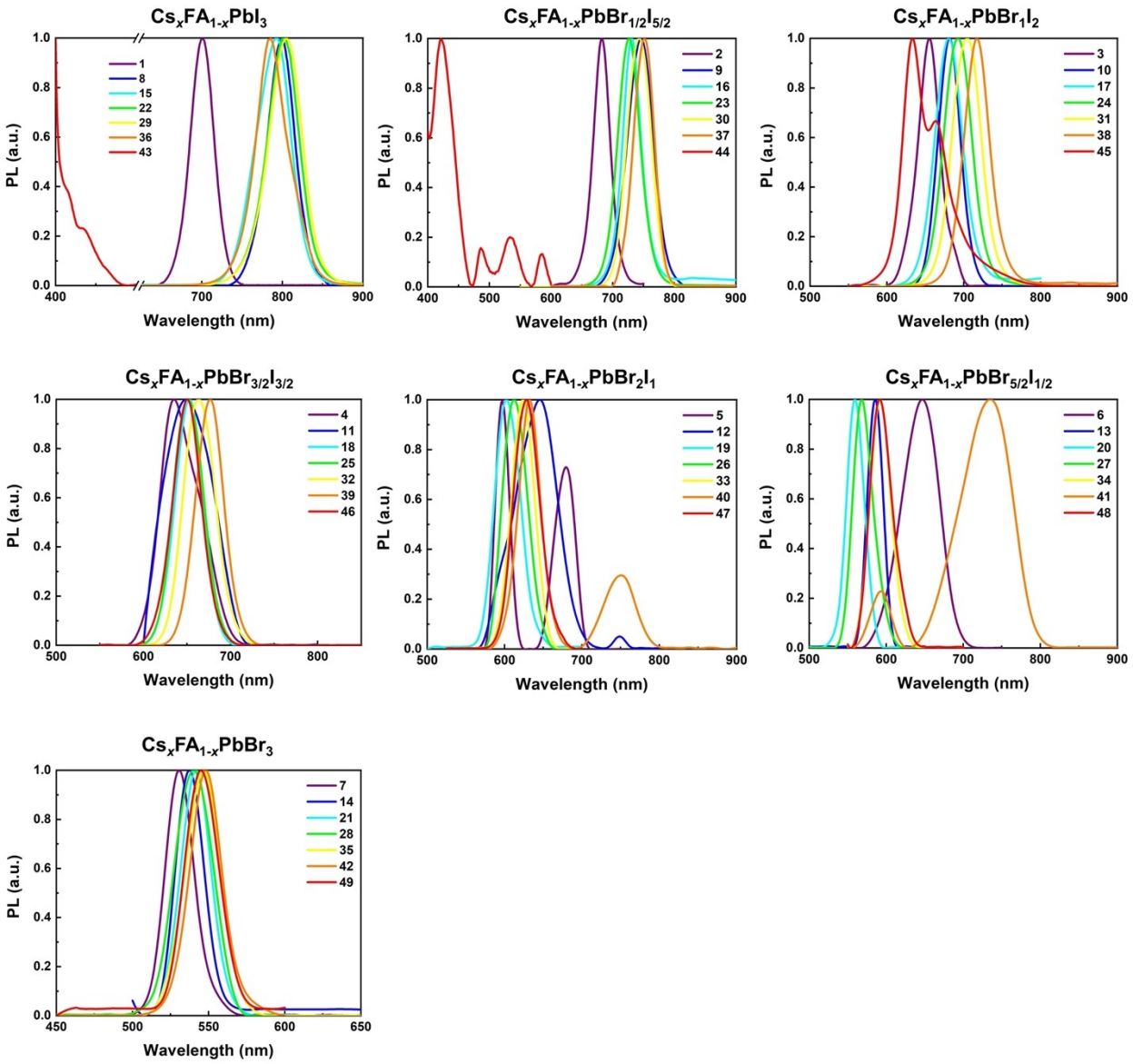

Fig. S18 Normalized photoluminescence spectra as a function of wavelength. Each figure represents a fixed Br/I ratio and a changing Cs/FA ratio, i.e. every column of the composition matrix.

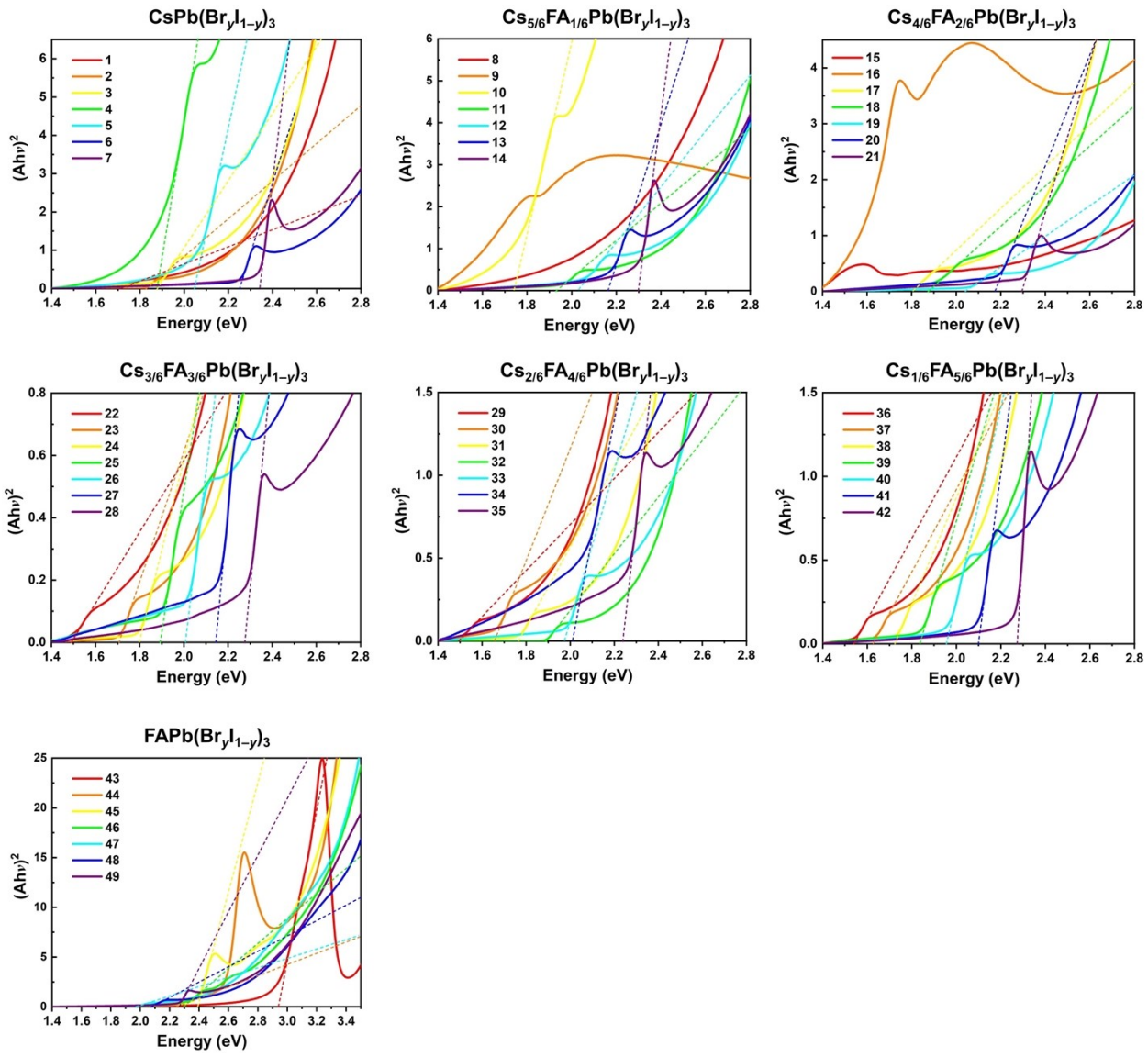

Fig. S19 Tauc plots based on the square of absorption as a function of photon energy. The bandgaps are determined by the intercept between the linear regions close to the absorption onset and the intercept. Each figure represents a fixed Cs/FA ratio and a changing Br/I ratio, i.e. every row of the composition matrix.

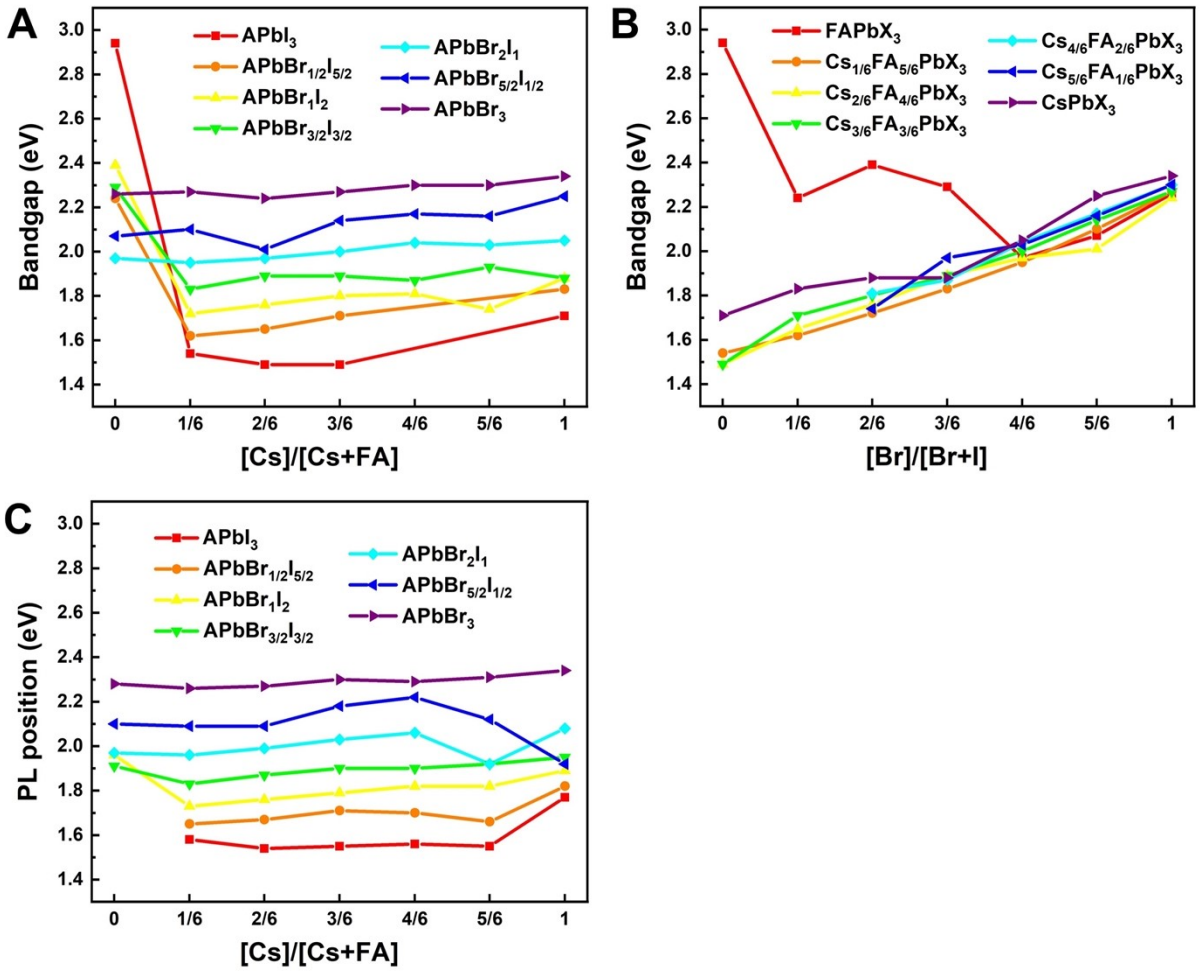

247

248 Fig. S20 Bandgaps as a function of Cs content (A) and Br content (B). Bandgap values were
249 calculated from Tauc plots in Fig. S18. (C) The PL energy extracted from the maximum emission
250 wavelength of PL as a function of Cs content.

251

Table. S1 Values of the coefficients in eqn. (2) of main text with 95% confidence bounds

Coefficient	Value	Standard error	Correlation
C_1	1.502	0.033	0.965
C_2	0.560	0.076	0.985
C_3	0.080	0.096	0.989
C_4	0.185	0.065	0.970
C_5	0.106	0.071	0.972
C_6	-0.097	0.063	0.939

Note:

1. The model of the fitting second-order polynomial is $E_g(x, y) = C_1 + C_2 \cdot x + C_3 \cdot y + C_4 \cdot x^2 + C_5 \cdot y^2 + C_6 \cdot x \cdot y$. The eqn. (2) was fitted by Origin software.
2. R-square value is also known as the coefficient of determination. The closer the fit is to the data points, the closer r-square will be to the value of 1. A larger value of r-square does not necessarily mean a better fit because the degree of freedom can also affect the value. Thus if more parameters are introduced, the r-square value will rise, but this does not imply a better fit. The adjusted r-square value accounts for the degrees of freedom to provide a better measure of the goodness of fit.

Device performance

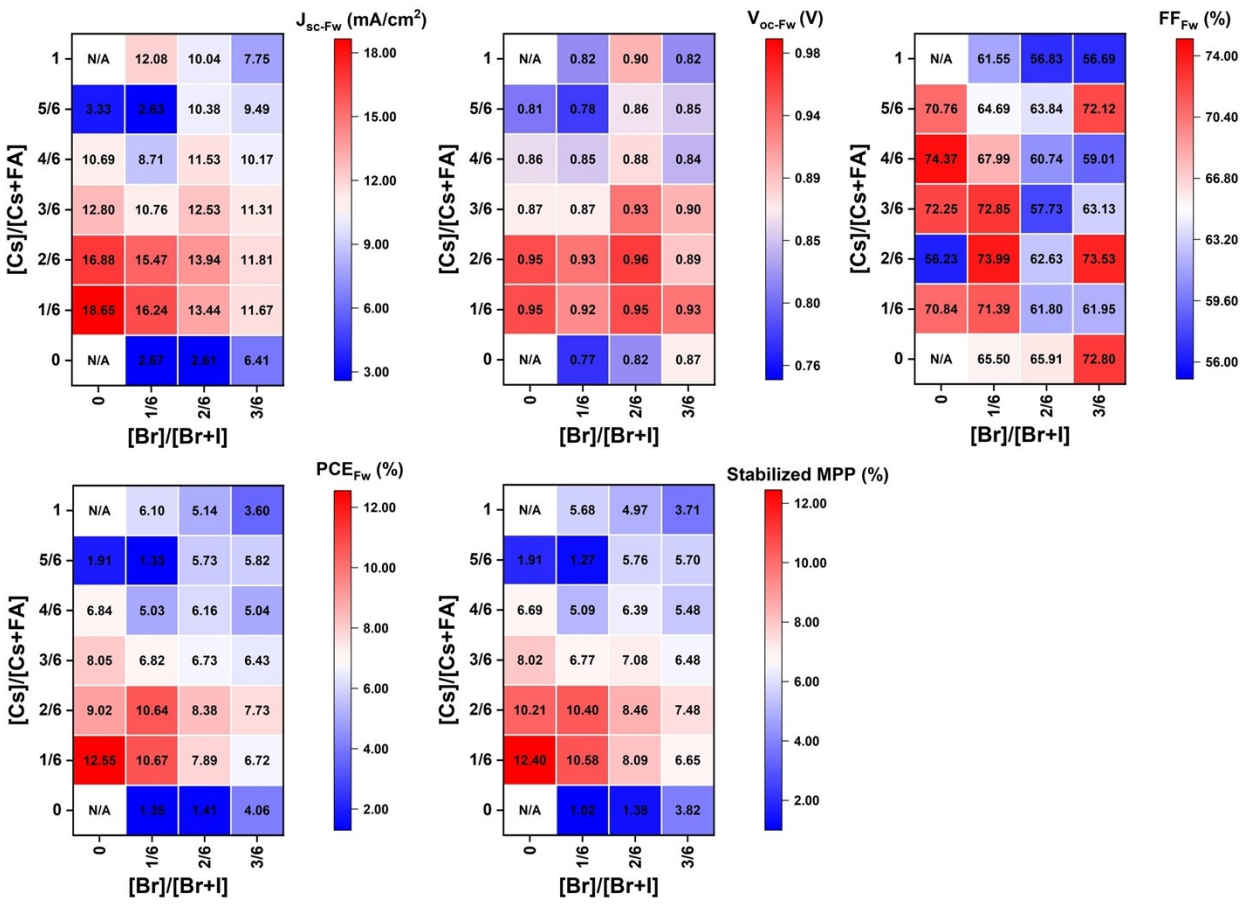

Fig.S21 The photovoltaic parameters of J_{sc}, V_{oc}, FF, and PCE for forward scan and stabilized power output at MPP attained from best devices of I-rich compositions using 0.4 M perovskite precursor solutions.

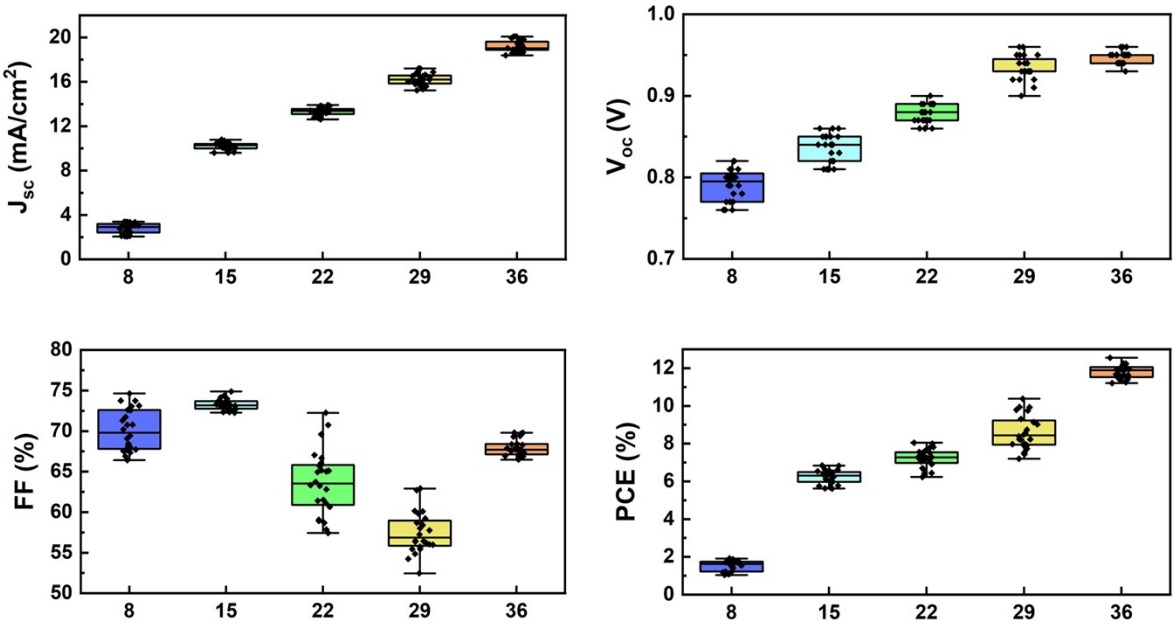

Fig.S22 Box plots of the photovoltaic parameters of the perovskite solar cells with composition $Cs_yFA_{1-y}PbI_3$.

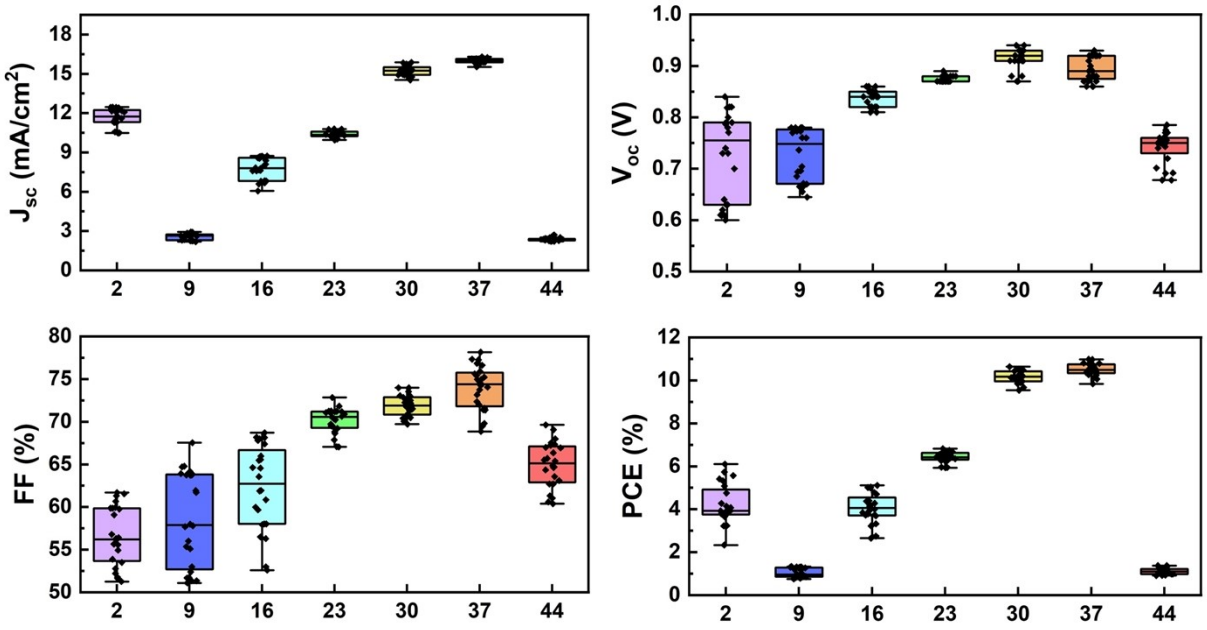

Fig.S23 Box plots of the photovoltaic parameters of the perovskite solar cells with composition $Cs_yFA_{1-y}PbBr_{1/2}I_{5/2}$.

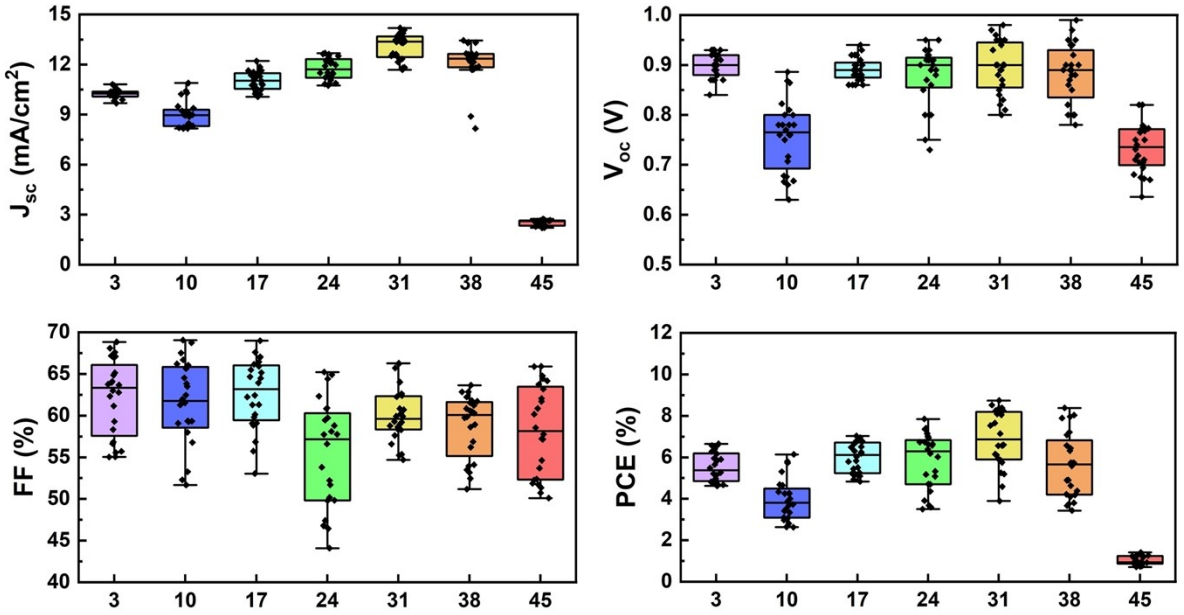

Fig.S24 Box plots of the photovoltaic parameters of the perovskite solar cells with composition $Cs_yFA_{1-y}PbBr_1I_2$.

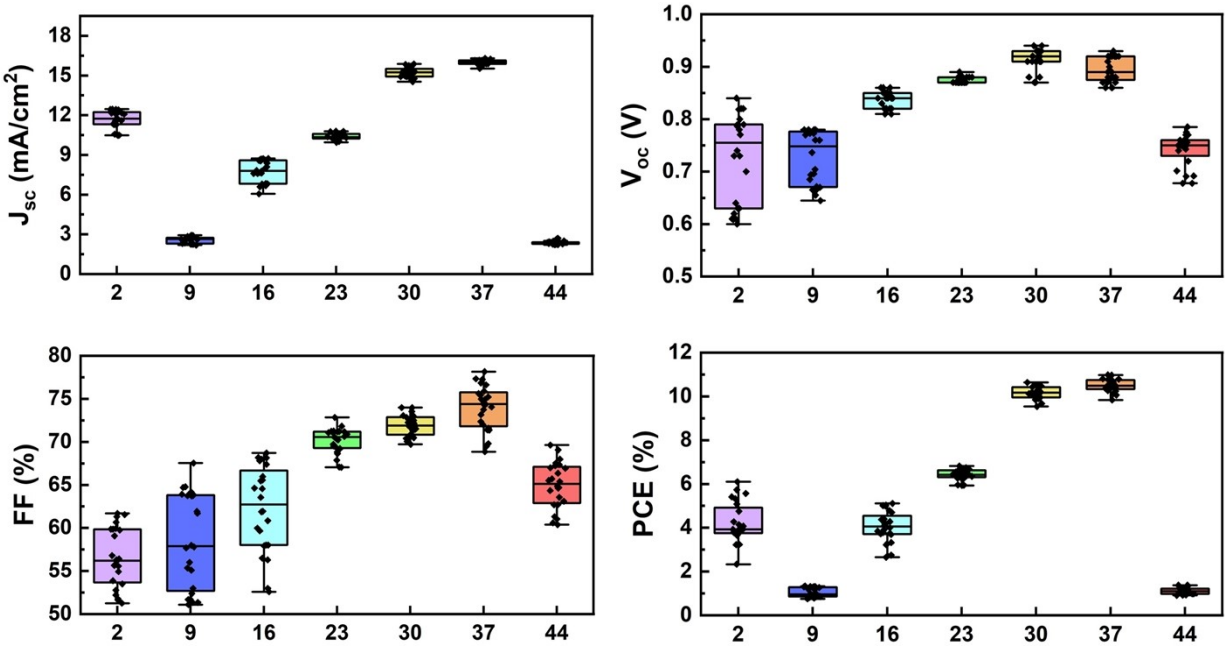

Fig.S25 Box plots of the photovoltaic parameters of the perovskite solar cells with composition $Cs_yFA_{1-y}PbBr_{3/2}I_{3/2}$.

Note 1: Additional discussions on texture:

The texture of perovskite crystallites within a film have been proposed to affect the charge carrier transport and collection properties across the layer, thus influencing the overall photovoltaic performance of the solar cell stack [14,15]. XRD highlighted a high level of texturing in our films, as mentioned above, resulting in prominent peaks at ~14° and ~28°. The reason for the orientation can be traced back to different surface energies for different planes [14]. The texture of a film can also be monitored looking at the GIWAXS diffraction patterns, tracking the intensity variations of a specific plane with varying azimuthal angle. The ring at q = 1.035 ± 0.09 Å in GIWAXS corresponds to the peak at ~14° in XRD, and is assigned to the $(100)_C$ plane for a cubic structure, to the $(110)_T$, $(001)_T$ reflections for the tetragonal phase, and to the $(110)_O$, $(002)_O$ reflections for the orthorhombic phase. The peak is integrated and plotted as function of the azimuthal angle as detailed in Fig. S26. Fig. S27summarizes the preferred facet orientation, as extracted from Fig.S26. All the 26 I-rich compositions show preferred facet orientation of crystal plane at peak q = 1.035 ± 0.09 Å, parallel to the substrate (0°) or/and stacked along the 45° direction with respect to the substrate (Fig. S26-S27). This indicates the ordered and long-range-orientated crystallization of the nineteen I-rich films, which is beneficial for charge transport within the perovskite films, and consequently device performance [16]. In addition, Fig. S28 schematically demonstrates $(100)_C$, $(110)_T$, $(001)_T$, $(110)_O$, and $(002)_O$ crystal planes, involve only one kind of stacking layer, composed of Pb and X atoms without A, regardless of the crystal phase. Therefore, the nineteen I-rich films are long-range-orientated and have same atomic stacking structure for the plane at peak q = 1.035 ± 0.09 Å. The azimuthal angle integration also shows the perovskite films for Cs-rich compositions are more oriented at 0° than that of FA-rich samples, suggesting higher texture of Cs-rich compositions, as illustrated in Fig. S26. However, the PCE of Cs-rich compositions is significantly lower than that of FA-rich compositions. Hence, the impact of the texture on the device performance is negligible in the face of other factors, e.g., bandgap, surface morphology, and the existence of δ-phase.

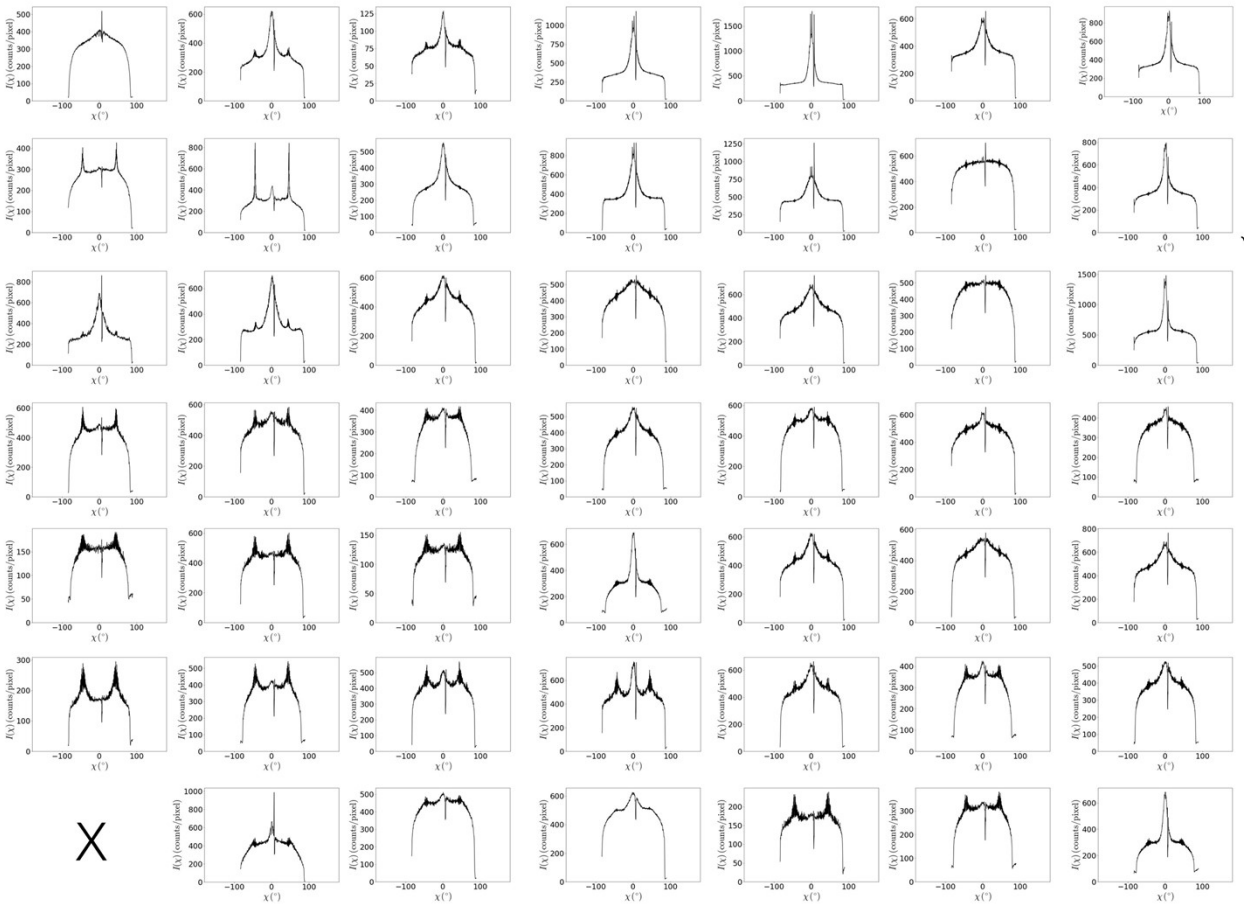

Fig. S26 Integrated azimuthal angle along the ring q (q = 1.035 ± 0.09 Å) at an incident angle of 0.5° corresponding to the location ~14° in XRD, assigned to (100) plane for a cubic structure, which plane splits into the (110), (001) reflections and (110), (002) reflections in the tetragonal phase and orthorhombic phase, respectively [17].

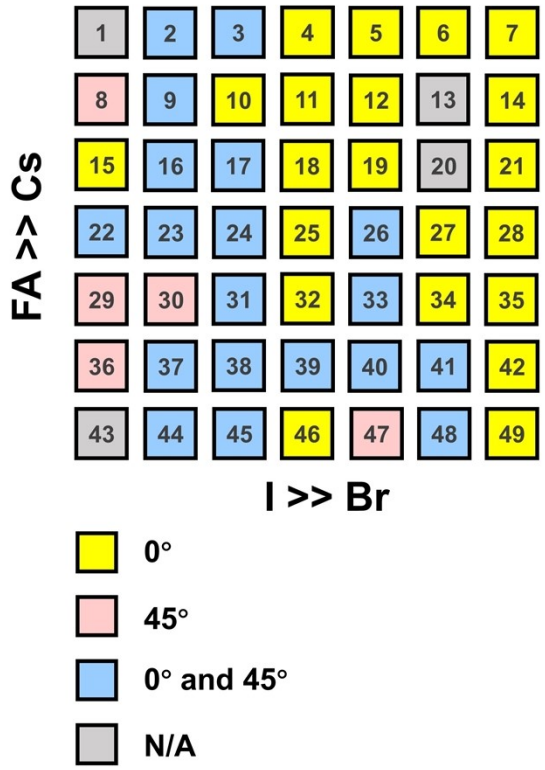

323

324 Fig. S27 Color map of the preferential integrated azimuthal angle along the ring q (q = 1.035 ±

325 0.09 Å) to summarize Fig. S25.

326

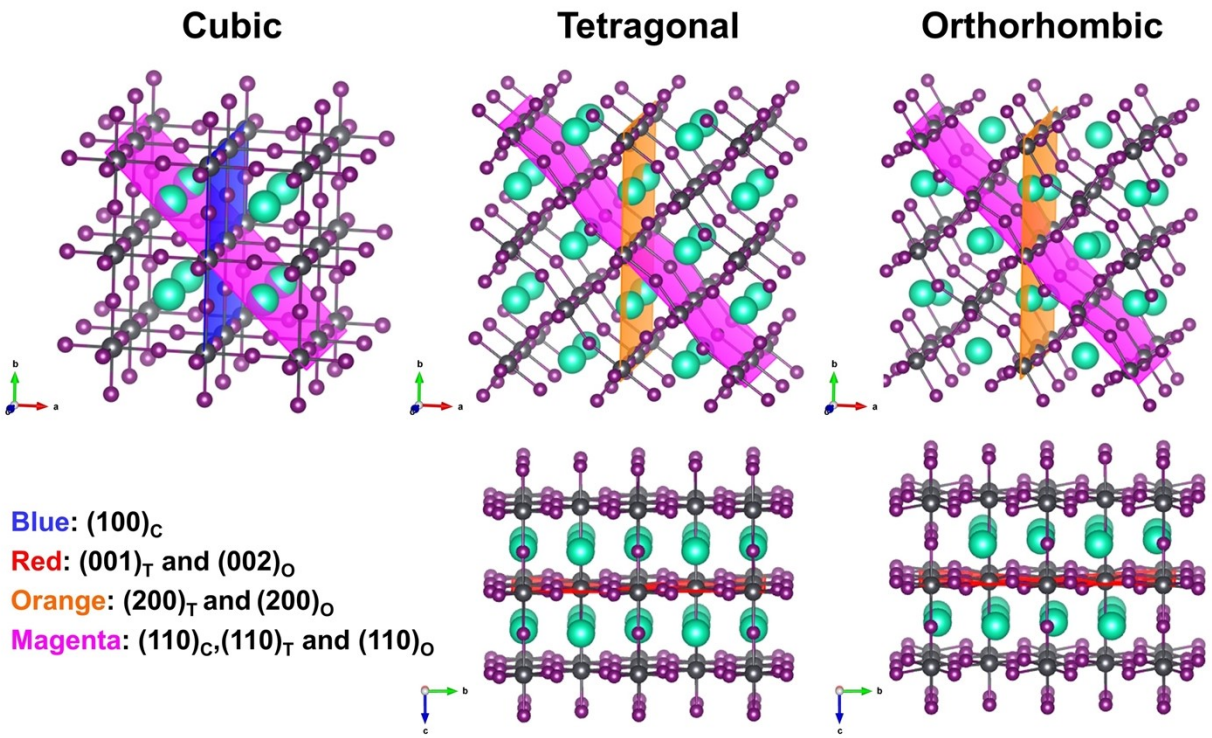

Fig. S28 Crystal structure models of three perovskite phases, including cubic, tetragonal and orthorhombic structure for different planes.

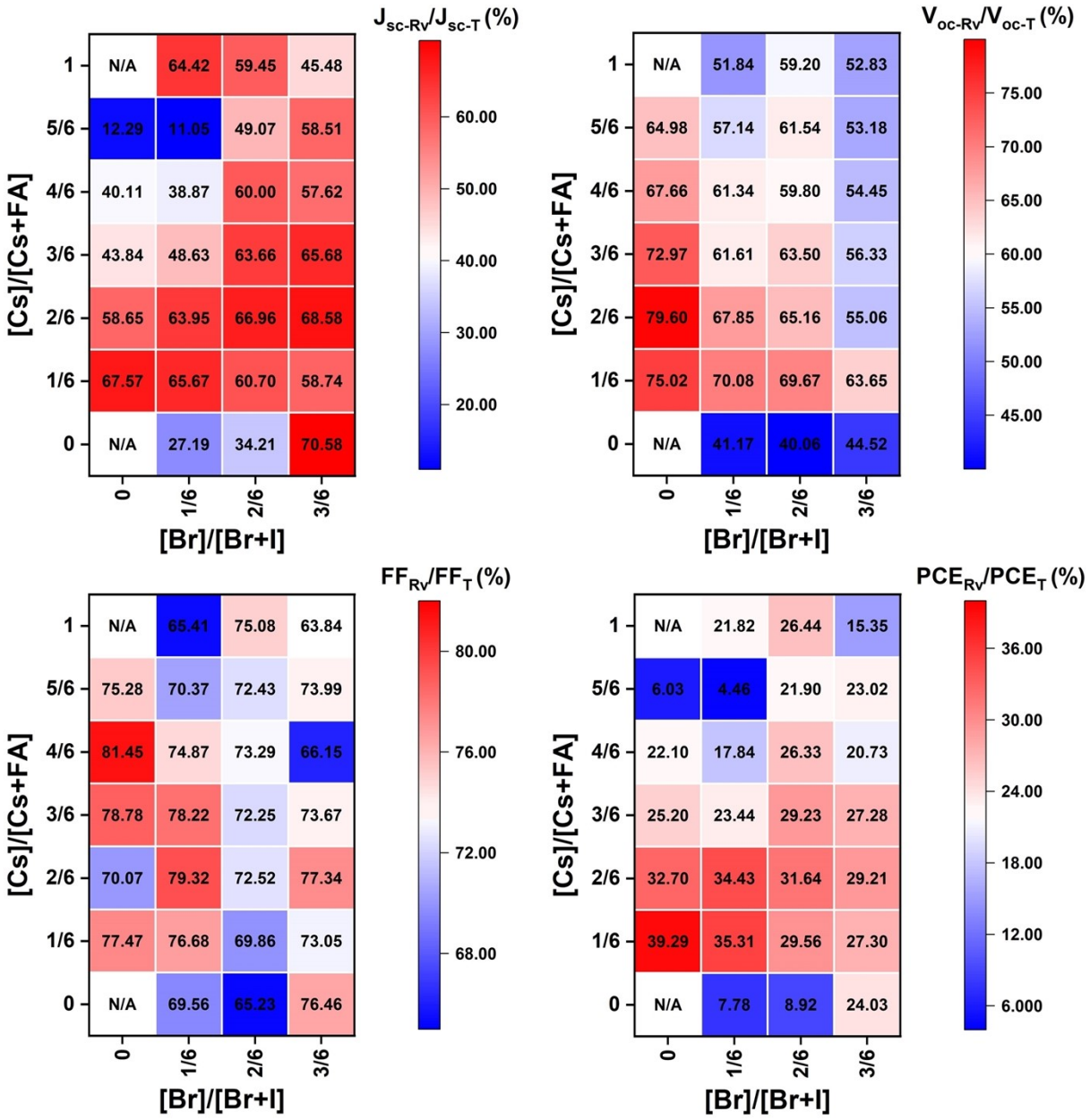

333

334 Fig.S29 The ratio of photovoltaic parameters of J_{sc}, V_{oc}, FF, and PCE for reverse scan from best
335 devices of I-rich compositions using 0.4 M perovskite precursor solutions to the corresponding
336 theoretical Shockley-Queisser limit [18].

337

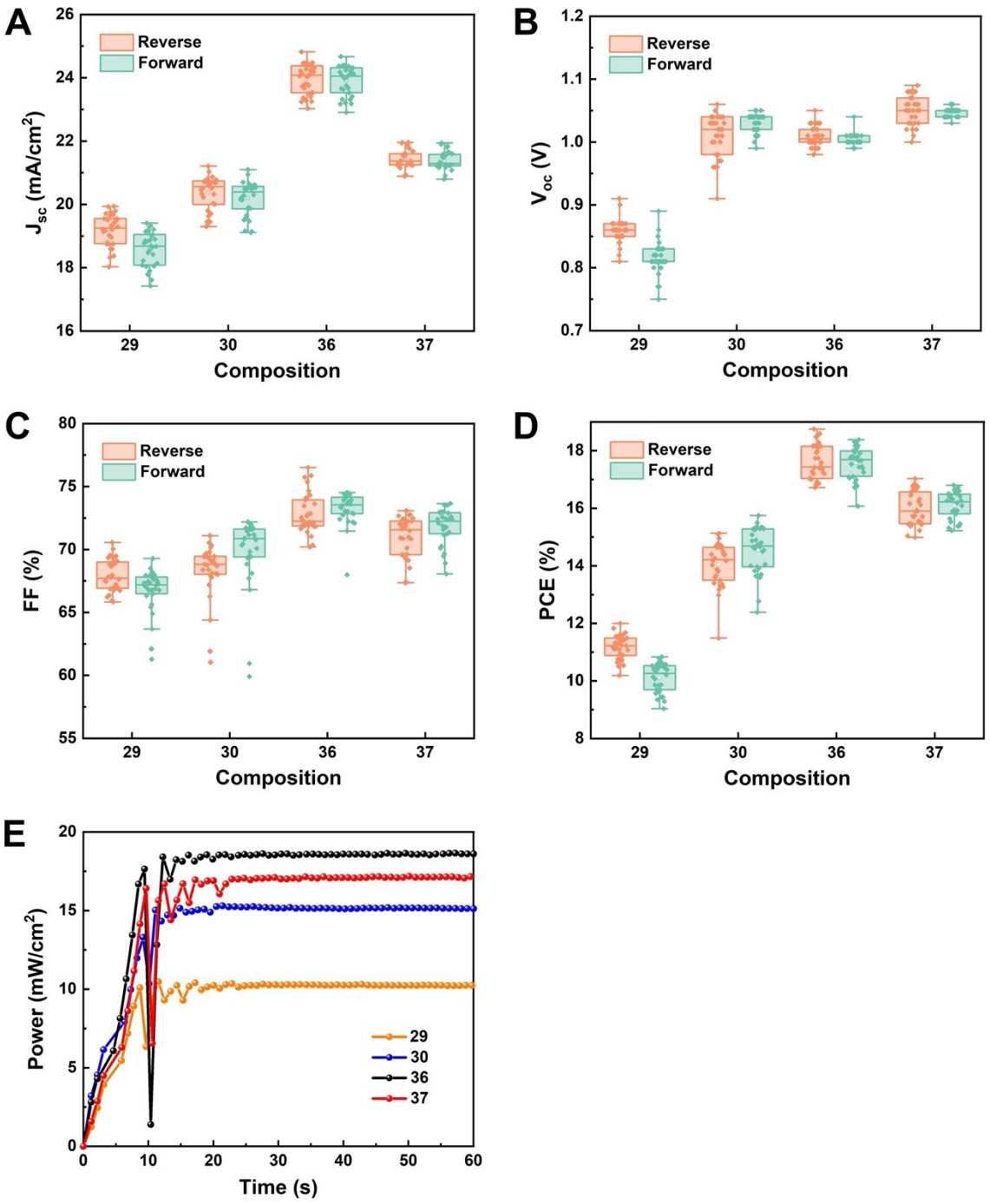

Fig.S30 Box plots for photovoltaic parameters of J_{sc} (A), V_{oc} (B), FF (C), and PCE (D) using 1.0 M perovskite precursor solutions for composition No 29, No.30, No.36, and No37. (E) The MPP tracking for the champion devices.

344

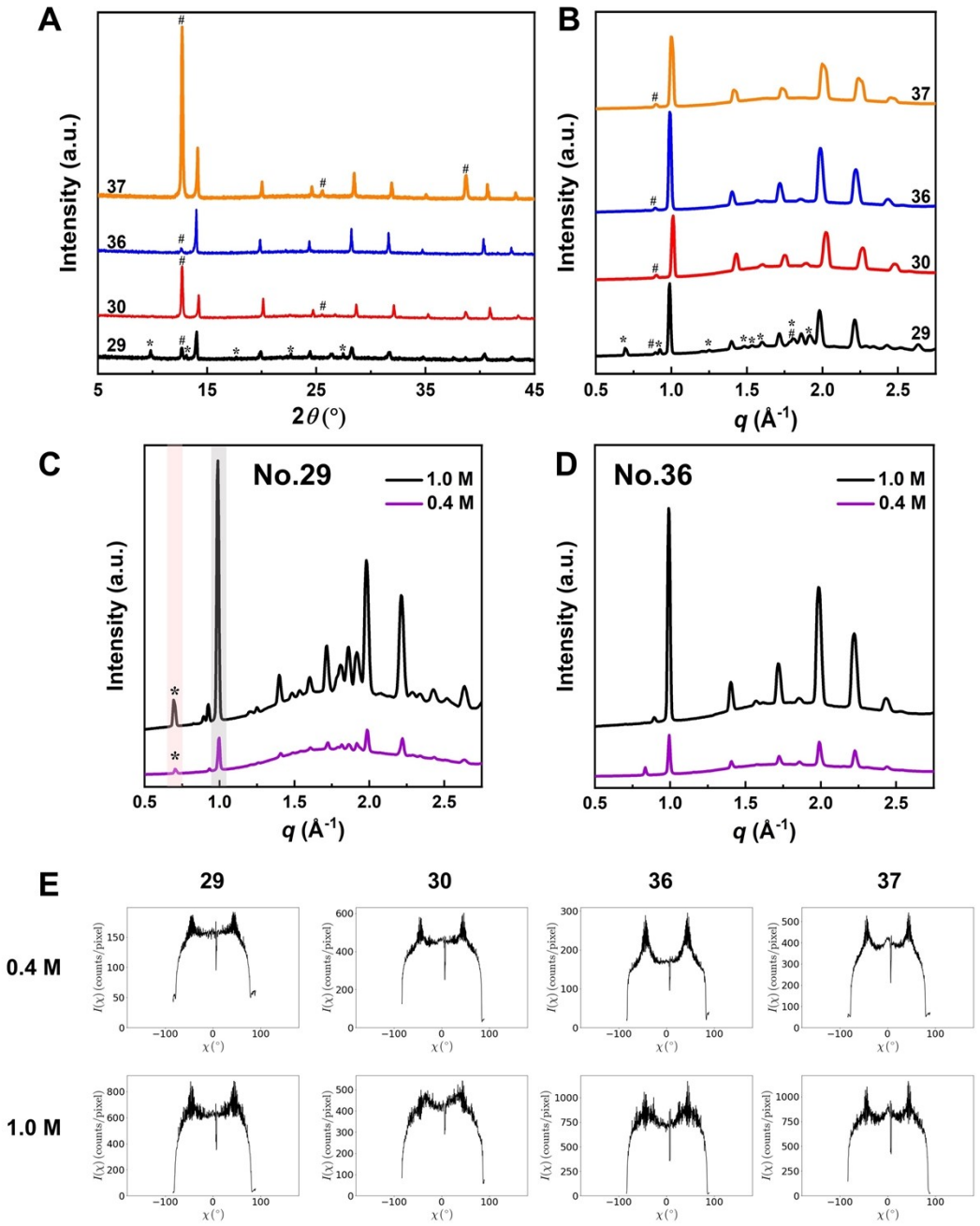

345

346 Fig.S31 XRD (A) and circular average of GIWAXS (B) patterns for composition No.29, No.30,
347 No.36, and No37 using 1.0 M perovskite precursor solutions along with the150 ℃ annealing. The
348 # and ∗ denote δ-$CsPbI_3$ and excess PbI_2, respectively. The GIWAXS comparison of the films with
349 composition No.29 (C) and No. 36 (D) deposited by 0.4 M precursors solution annealing at 65℃
350 and by 1.0 M precursors solution annealing at 150℃. (E) Integrated azimuthal angle for

351 composition No.29, No.30, No.36, and No37, deposited by 0.4 M precursors solution annealing at
352 65℃ and by 1.0 M precursors solution annealing at 150℃, along the ring q (q = 1.035 ± 0.09 Å)
353 at an incident angle of 0.5° corresponding to the location ~14° in XRD, assigned to (100) plane
354 for a cubic structure, which plane splits into the (110), (001) reflections in the tetragonal phase.
355

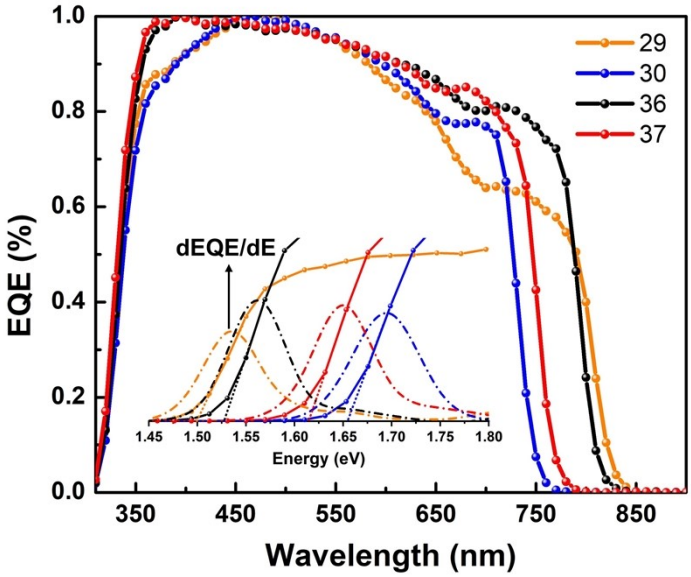

Fig. S32 EQE spectra of the perovskite solar cell for No.29, N0.30, No.36, and No.37. The insert showed the photovoltaic bandgap extracted from extrapolation to 0 of the EQE curve or the inflection point of the derivative of the EQE curve.

Table S2. Optical bandgap extracted from absorbance (E_g) and PL (E_{PL}) as well as the photovoltaic bandgap extracted from EQE spectra measured by solar cells using the extrapolation to 0 of the EQE curve (E_0) or the inflection point of the derivative of the EQE curve (E_{IP}).

Composition	29	30	36	37
E_g/eV	1.49	1.65	1.54	1.62
E_{PL}/eV	1.54	1.67	1.58	1.65
E_0/eV	1.50	1.65	1.53	1.61
E_{IP}/eV	1.53	1.70	1.56	1.65

Note: For the mismatch between optical bandgap and photovoltaic bandgap, the optical bandgap determined by the Tauc method represents an internal property of the photovoltaic material while the photovoltaic bandgap determined by the EQE represents an external property of the solar cells. In practice, the device structure and fabrication methods may modify the optoelectronic properties of the device, producing a mismatch between the optical value and photovoltaic bandgap [19,20].

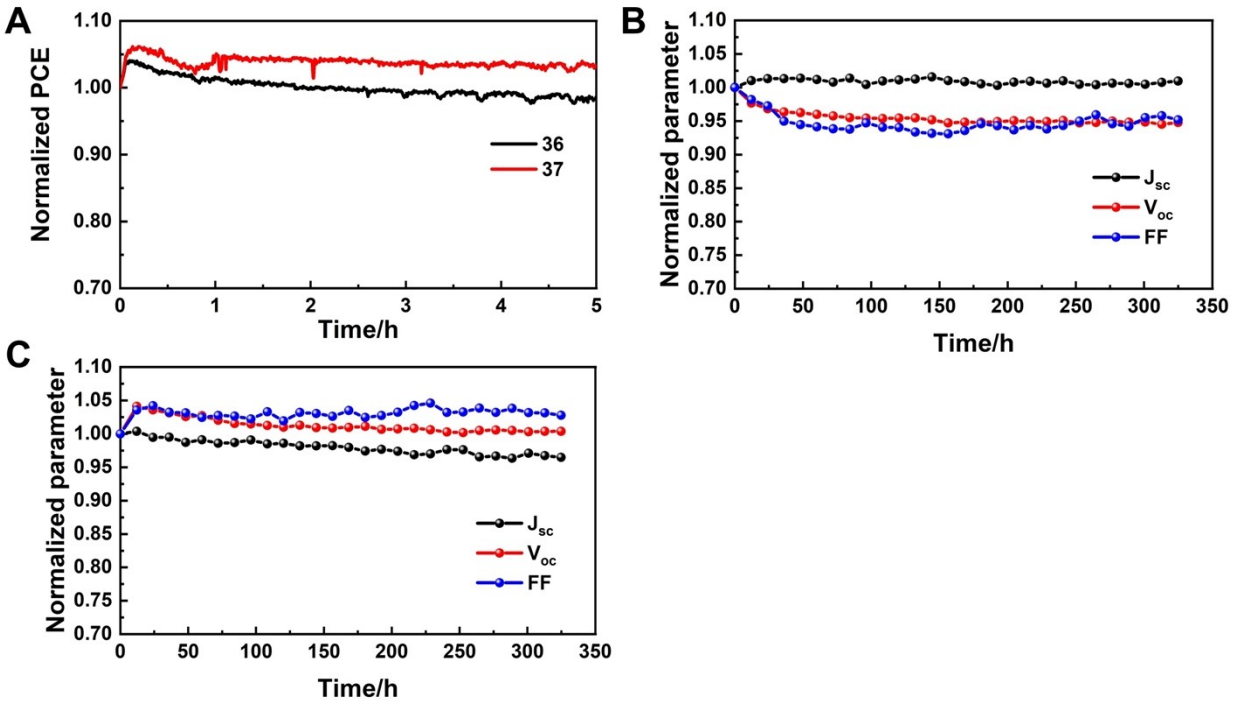

371

372 Fig.S33 (A) Continuous MPP tracking results under 1 sun irradiance at N_2 atmosphere of devices
373 of composition 36 and 37 for first 5 hours, which was zoomed from the Fig 10 F in the main text.
374 The evolution of the normalized V_{oc}, $J_{sc,}$ and FF of PSCs for composition No.36 (B) and No.37
375 (C) that aged under at MPP with 1 sun irradiation in N_2 atmosphere at room temperature.

376

377

Reference

1 J. P. Perdew, A. Ruzsinszky, G. I. Csonka, O. A. Vydrov, G. E. Scuseria, L. A. Constantin, X. Zhou and K. Burke, *Phys. Rev. Lett.*, 2008, **100**, 136406.

2 P. E. Blöchl, *Phys. Rev. B*, 1994, **50**, 17953–17979.

3 D. Joubert, *Phys. Rev. B - Condens. Matter Mater. Phys.*, 1999, **59**, 1758–1775.

4 W. A. Saidi and J. J. Choi, *J. Chem. Phys.*, 2016, **145**, 144702.

5 A. Tkatchenko and M. Scheffler, *Phys. Rev. Lett.*, 2009, **102**, 073005.

6 W. A. Al-Saidi, V. K. Voora and K. D. Jordan, *J. Chem. Theory Comput.*, 2012, **8**, 1503–1513.

7 W. Shan and W. A. Saidi, *J. Phys. Chem. Lett.*, 2017, **8**, 5935–5942.

8 W. A. Saidi, W. Shadid and I. E. Castelli, *npj Comput. Mater.*, 2020, **6**, 1–7.

9 C. C. Stoumpos, C. D. Malliakas and M. G. Kanatzidis, *Inorg. Chem.*, 2013, **52**, 9019–9038.

10 B. Zhao, S. F. Jin, S. Huang, N. Liu, J. Y. Ma, D. J. Xue, Q. Han, J. Ding, Q. Q. Ge, Y. Feng and J. S. Hu, *J. Am. Chem. Soc.*, 2018, **140**, 11716–11725.

11 A. Marronnier, G. Roma, S. Boyer-Richard, L. Pedesseau, J.-M. M. Jancu, Y. Bonnassieux, C. Katan, C. C. Stoumpos, M. G. Kanatzidis and J. Even, *ACS Nano*, 2018, **12**, 3477–3486.

12 M. Rodová, J. Brožek, K. Knížek and K. Nitsch, *J. Therm. Anal. Calorim.*, 2003, **71**, 667–673.

13 G. A. Elbaz, D. B. Straus, O. E. Semonin, T. D. Hull, D. W. Paley, P. Kim, J. S. Owen, C. R. Kagan and X. Roy, *Nano Lett.*, 2017, **17**, 1727–1732.

14 Z. Xu, Z. Liu, N. Li, G. Tang, G. Zheng, C. Zhu, Y. Chen, L. Wang, Y. Huang, L. Li, N. Zhou, J. Hong, Q. Chen and H. Zhou, *Adv. Mater.*, 2019, **31**, 1900390.

15 J. Hidalgo, C. A. R. Perini, A. F. Castro-Mendez, D. Jones, H. Köbler, B. Lai, R. Li, S. Sun, A. Abate and J. P. Correa-Baena, *ACS Energy Lett.*, 2020, **5**, 3526–3534.

16 G. Zheng, C. Zhu, J. Ma, X. Zhang, G. Tang, R. Li, Y. Chen, L. Li, J. Hu, J. Hong, Q. Chen, X. Gao and H. Zhou, *Nat. Commun.*, 2018, **9**, 1–11.

17 J. A. Vigil, A. Hazarika, J. M. Luther and M. F. Toney, *ACS Energy Lett.*, 2020, **5**, 2475–2482.

18 S. Rühle, *Sol. Energy*, 2016, **130**, 139–147.

19 O. Almora, C. I. Cabrera, J. Garcia-Cerrillo, T. Kirchartz, U. Rau and C. J. Brabec, *Adv. Energy Mater.*, 2021, **11**, 2100022.

20 L. Krückemeier, U. Rau, M. Stolterfoht and T. Kirchartz, *Adv. Energy Mater.*, 2020, **10**, 1902573.